

November 2014

# UBOT-7: THE DESIGN OF A COMPLIANT DEXTEROUS MOBILE MANIPULATOR

Jonathan Cummings  
*University of Massachusetts Amherst*

Follow this and additional works at: [https://scholarworks.umass.edu/masters\\_theses\\_2](https://scholarworks.umass.edu/masters_theses_2)



Part of the [Controls and Control Theory Commons](#), [Electro-Mechanical Systems Commons](#), and the [Robotics Commons](#)

---

## Recommended Citation

Cummings, Jonathan, "UBOT-7: THE DESIGN OF A COMPLIANT DEXTEROUS MOBILE MANIPULATOR" (2014). *Masters Theses*. 78.  
[https://scholarworks.umass.edu/masters\\_theses\\_2/78](https://scholarworks.umass.edu/masters_theses_2/78)

This Open Access Thesis is brought to you for free and open access by the Dissertations and Theses at ScholarWorks@UMass Amherst. It has been accepted for inclusion in Masters Theses by an authorized administrator of ScholarWorks@UMass Amherst. For more information, please contact [scholarworks@library.umass.edu](mailto:scholarworks@library.umass.edu).

**UBOT-7: THE DESIGN OF A COMPLIANT DEXTEROUS MOBILE MANIPULATOR**

A Thesis Presented

by

JONATHAN P CUMMINGS

Submitted to the Graduate School of the  
University of Massachusetts Amherst in partial fulfillment  
of the requirements for the degree of

MASTERS OF SCIENCE IN MECHANICAL ENGINEERING

SEPTEMBER 2014

MECHANICAL AND INDUSTRIAL ENGINEERING

© Copyright by Jonathan P Cummings 2014

All Rights Reserved

# **UBOT-7: THE DESIGN OF A COMPLIANT DEXTEROUS MOBILE MANIPULATOR**

A Thesis Presented

by

JONATHAN P CUMMINGS

Approved as to style and content by:

---

Frank C. Sup IV, Chair

---

Roderic A. Grupen, Member

---

James R. Rinderle, Member

---

Donald L. Fisher, Department of Mechanical and  
Industrial Engineering

## **DEDICATION**

I would like to dedicate this thesis to my parents, Andrea Tosi and Steve Cummings. They have been a constant source of motivation and support through my entire life. Without them I would not have been able to have finished the work that I have. I would also like to dedicate this to the rest of my family, especially Morgan and Sam, and friends that have helped me every step of the way throughout my life and education.

## **ACKNOWLEDGMENTS**

Firstly, I would like to thank my Advisor, Professor Frank Sup. He has provided me with the guidance and support necessary to succeed over the past two years. Because of him I have gained much knowledge that has helped build my skills as a mechanical engineer and roboticist. I would also like to thank Professor Rod Grupen for his guidance throughout my experience at UMass. Because I spent my time divided between his lab, The Laboratory of Perceptual Robotics, and the Mechatronics and Robotics Research Laboratory, he has taught me many lessons that will extend beyond the development of the uBot-7. Additionally, I would like to thank Professor James Rinderle because he has provided me with insight into practices that will make me a better engineer.

I would also like to thank all of the students in both the LPR and MRRL as I have learned as much from them as I have from any other source in the university. They have provided me with both knowledge and a work environment that I enjoyed being part of.

## **ABSTRACT**

UBOT-7: THE DESIGN OF A COMPLIANT DEXTEROUS MOBILE MANIPULATOR

SEPTEMBER 2014

JONATHAN P. CUMMINGS, B.S., RENSSELAER POLYTECHNIC INSTITUTE

M.S.M.E., UNIVERSITY OF MASSACHUSETTS AMHERST

Directed by: Professor Frank C. Sup IV

This thesis presents the design of uBot-7, the latest version of a dexterous mobile manipulator. This platform has been iteratively developed to realize a high performance-to-cost dexterous whole body manipulator with respect to mobile manipulation. The semi-anthropomorphic design of the uBot is a demonstrated and functional research platform for developing advanced autonomous perception, manipulation, and mobility tasks. The goal of this work is to improve the uBot's ability to sense and interact with its environment in order to increase the platforms capability to operate dexterously, through the incorporation of joint torque feedback, and safely, through the implementation of passive and active compliance. This is accomplished through incorporating series elastic actuators in its arms and torso joints, improving the mechanical design to reduce backlash, and incorporating impedance controllers in the robot. The focus of this thesis is the development of the mechanical, sensor, and controller design for the uBot-7 platform. An impedance controller is developed and evaluated on a bench top prototype series elastic actuator.

## TABLE OF CONTENTS

	Page
ACKNOWLEDGMENTS.....	v
ABSTRACT.....	vi
LIST OF TABLES.....	ix
LIST OF FIGURES.....	x
CHAPTER	
1 INTRODUCTION.....	1
1.1 Research Motivation.....	1
1.2 Research Scope .....	2
1.3 Thesis Outline .....	5
2 BACKGROUND.....	6
2.1 uBot Overview .....	6
2.2 Series Elastic Actuation (SEA) .....	12
2.3 Compliant Humanoids .....	16
2.3.1 Robonaut 2.....	18
2.3.2 COMAN .....	21
3 MECHANICAL DESIGN OF UBOT-7 .....	24
3.1 Design Requirements.....	25
3.2 SEA Mechanism Overview .....	29
3.3 Selection of DC Motors and Gearheads.....	32
3.4 Spring Design .....	35
3.5 Selection of Spring Constants .....	37
3.6 Arm Design.....	40
3.6.1 Shoulder Flexion .....	41
3.6.2 Shoulder Abduction .....	43
3.6.3 Shoulder Twist .....	45
3.6.4 Elbow .....	48
3.7 Torso Design.....	50
3.8 Drivetrain Design .....	52
3.9 Distributed Embedded System .....	54
3.10 uBot-7 Mechanical Design Summary.....	57
4 SENSOR DESIGN .....	60
4.1 Spring Deflection Sensor.....	61
4.2 Deflection Sensor Design Steps .....	64
4.3 Experimental Validation.....	66
4.4 Absolute Position Sensor .....	67
5 CONTROLLER DESIGN.....	69
5.1 System Model .....	70
5.2 Impedance Controller .....	71
5.3 Torque Controller.....	72
5.4 Controller Hardware .....	73
6 IMPLEMENTATION AND EXPERIMENTS .....	75
6.1 Torque Controller Evaluation.....	75
6.2 Impedance Controller Evaluation .....	80



7	RECOMMENDATIONS FOR FUTURE IMPLEMENTATION.....	84
8	CONCLUSION.....	86
	APPENDIX: EXPERIMENTAL PARAMETER VALUES .....	88
	REFERENCES.....	91

## LIST OF TABLES

Table	Page
<b>2.1</b> uBot-5 actuator peak torques, no load speeds, and mechanisms .....	9
<b>2.2</b> uBot-6 actuator peak torques, no load speeds, and mechanisms .....	9
<b>2.3</b> uBot-5 & 6 weight and dimensions.....	11
<b>3.1</b> uBot-7 Design Requirements .....	27
<b>3.2</b> uBot-7 joint maximum torque and no load speed compared to the values determined from functional requirements .....	33
<b>3.3</b> uBot-6 and uBot-7 joint torque and speed specifications. The red boxes indicated the a change of over a factor of 2, the yellow boxes indicate a smaller change, and the green boxes indicate the value is approximately the same .....	34
<b>3.4</b> uBot-7 actuators peak torques, no-load speeds, spring constants, and motor-gearhead combinations .....	39
<b>3.5</b> uBot-7 SEA joint natural frequencies.....	39
<b>3.6</b> Tightening torque for spring screws [47].....	39
<b>3.7</b> uBot-6 and uBot-7 size and weight (*based on CAD model not actual weight).....	58

## LIST OF FIGURES

Figure	Page
<b>1.1</b> uBot-6 [5] .....	2
<b>2.1</b> uBot-5 [4] .....	6
<b>2.2</b> iRobot's PackBot is a good example of a traditional mobile robot that has a low center of mass and a large footprint [17] .....	7
<b>2.3</b> uBot-5 learning dynamic arm motions for postural recovery [18] .....	8
<b>2.4</b> uBot-6 in knuckle walking mobility mode.....	9
<b>2.5</b> The different postural modes uBot-6 can attain to accomplish a goal [5] .....	10
<b>2.6</b> Schematic of series elastic actuator .....	12
<b>2.7</b> Rethink Robotics' Baxter™[32] .....	16
<b>2.8</b> NASA's Robonaut 2 [15].....	18
<b>2.9</b> Springs used in Robonaut 2's SEAs [15] .....	19
<b>2.10</b> Compliant HuMANoid Platform from IIT [34] .....	21
<b>2.11</b> COMAN's series elastic actuators featuring a custom spring design, and torque load cell [22] .....	22
<b>3.1</b> Rendering of the uBot-7 CAD model.....	24
<b>3.2</b> uBot moving shoulder abduction joint 180° .....	26
<b>3.3</b> uBot doing a pushup .....	26
<b>3.4</b> uBot holding a weight in multiple configurations.....	26
<b>3.5</b> Prototype SEA developed for design validation .....	29
<b>3.6</b> Cross-section of prototype SEA joint for uBot-7 .....	30
<b>3.7</b> SEA prototype without deflection sensor or cover to show spring used .....	31
<b>3.8</b> Spring geometry used in uBot-7. [16,45]. The discoloration is a result of the heat treatment process.....	35
<b>3.9</b> Spring constant from FEA simulation vs. material thickness.....	36

<b>3.10</b>	Factor of safety plot from FEA simulation of SEA prototype spring at 4° of deflection .....	38
<b>3.11</b>	Rendering of uBot-7 arm CAD model .....	40
<b>3.12</b>	uBot-6 shoulder flexion joint .....	41
<b>3.13</b>	uBot-7 shoulder flexion joint, cross-sectional view of joint, and keyless tapered bushing used [48] .....	42
<b>3.14</b>	uBot-6 shoulder abduction joint.....	43
<b>3.15</b>	uBot-7 shoulder abduction joint.....	44
<b>3.16</b>	uBot-6 shoulder twist shaft connector clamp .....	45
<b>3.17</b>	uBot-6 shoulder twist joint .....	46
<b>3.18</b>	uBot 7 shoulder twist joint and the tapered bushing used [49] .....	47
<b>3.19</b>	uBot-6 elbow joint .....	48
<b>3.20</b>	uBot-7 elbow joint .....	49
<b>3.21</b>	uBot-6 torso joint.....	50
<b>3.22</b>	uBot-7 torso joint.....	51
<b>3.23</b>	uBot-6 drivetrain mechanism .....	52
<b>3.24</b>	uBot-7 drivetrain Mechanism .....	53
<b>3.25</b>	Layout of uBot-6's embedded system .....	54
<b>3.26</b>	Outline of the uBot-7 distributed embedded system.....	55
<b>3.27</b>	Base and torso of uBot-7 .....	57
<b>3.28</b>	uBot-6 arm center of mass location .....	58
<b>3.29</b>	uBot-7 arm center of mass location .....	58
<b>4.1</b>	Deflection sensor configuration.....	62
<b>4.2</b>	Sensor movement (indicated by red arrows) within the magnet field of a rectangular neodymium magnet. The colors correspond to the magnitude of the magnetic flux density ( $ B $ ) of the field. Simulation done using FEMM software[50] .....	63
<b>4.3</b>	Normal magnetic flux density vs. position from simulation and experimentation on micrometer stage.....	63

<b>4.4</b>	<b>Magnetic Flux Density in the Z direction (normal to surface of ic) at maximum displacement (4mm) vs. air gap size.....</b>	<b>65</b>
<b>4.5</b>	<b>Micrometer stage setup used to test sensor.....</b>	<b>66</b>
<b>4.6</b>	<b>Absolution position sensor pulley configuration for uBot-7 shoulder flexion joint .....</b>	<b>67</b>
<b>4.7</b>	<b>Shoulder flexion joint sensor positions and phase shift between the sensors .....</b>	<b>68</b>
<b>5.1</b>	<b>SEA Model used to derive equations of motion .....</b>	<b>70</b>
<b>5.2</b>	<b>Impedance Controller Structure .....</b>	<b>71</b>
<b>5.3</b>	<b>Proposed schematic of local joint controller hardware structure.....</b>	<b>74</b>
<b>6.1</b>	<b>Torque Bode plot of SEA prototype with an input signal that has a magnitude of 1 Nm, 2 Nm, 4 Nm, and with only an open loop controller .....</b>	<b>76</b>
<b>6.2</b>	<b>Torque Bode plot of SEA prototype with spring constants of 3.6 Nm/° and 7.2 Nm/° .....</b>	<b>77</b>
<b>6.3</b>	<b>Torque Bode plot of actuator with 1 Nm magnitude sine wave centered at zero causing backlash and centered at 5 Nm eliminating backlash .....</b>	<b>78</b>
<b>6.4</b>	<b>Trajectory following at 1/2 Hz (top) and 1 Hz (bottom) with high and low impedances of <math>K_z=360</math> mNm/deg and <math>K_z=36</math> mNm/deg and a damping coefficient of <math>D_z=5</math>mNmS/deg .....</b>	<b>81</b>
<b>6.5</b>	<b>The SEA prototype with an object obstructing its trajectory (left) and after the object has been moved when using high impedance (right).....</b>	<b>81</b>
<b>6.6</b>	<b>¼ Hz trajectory following with <math>K_z=360</math> mNm/deg, <math>D_z=5</math>mNmS/deg (left) and <math>K_z=18</math> mNm/deg, <math>D_z=5</math>mNmS/deg and a collision at 5 seconds.....</b>	<b>82</b>
<b>6.7</b>	<b>Step response of the impedance controller to a 30° and 90° step at high, medium, and low stiffnesses of 360 mNm/deg, 180 mNm/deg, and 36 mNm/deg.....</b>	<b>83</b>

## CHAPTER 1

### INTRODUCTION

#### 1.1 Research Motivation

To expand the utility of robots in real world environments, two critical areas of research that need to be addressed are: dexterous manipulation and safe robot behavior [1], [2]. Pure manipulation occurs when an object is completely known. Pure exploration occurs when the object is fixtured and not known [3]. Dexterous manipulation is a combination of exploration and manipulation and can be thought of as an object centered manipulation in which multiple manipulators are in contact with the object. The object's desired motion can be used to determine the forces that the manipulators apply to that object. Because of this, incorporating joint torque feedback can be used to increase the dexterity of the robot. In order to make it possible for robots to share a work environment and interact with humans, it is very important that the robot is safe to work around. It is also important that the robot does not cause harm to itself while operating in an environment that is dynamic and not exhaustively modeled. Improving upon these two areas extends the general capability and utility of robots.

The areas of dexterity, and safety can only be developed from the proper implementation of effective software that is running on a capable hardware platform. Thus, it is critical that capable platforms exist in order to improve the field of robotics. To address these issues, the uBot platform has been developed in the Laboratory of Perceptual Robotics at the University of Massachusetts-Amherst. The latest version of the uBot, uBot-6, is shown in Figure 1.1. It is an embodiment of whole body dexterity with respect to mobile manipulation. This means that it uses multiple parts of its body, beyond its wheels and end effectors, to complete goals. It is a proven and useful research platform that has been through many design iterations. The platform has made contributions to the concepts of dexterous mobility [4]–[6], autonomous

skill acquisition [7], [8], emergency response [9], and even physical rehabilitation [10]–[13]. However, with increased focus on developing its capability to operate safely and dexterously, there is a need to further develop the systems hardware to accomplish this goal.

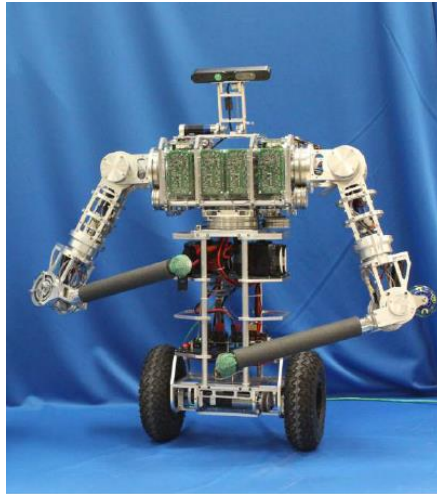


**Figure 1.1** uBot-6 [5]

## **1.2 Research Scope**

The goal of this work is to improve the capability of the uBot platform to perform manipulations and to operate as a safe mobile manipulator. This is done through the improvement of the system's hardware and focuses on the addition of joint torque feedback and the incorporation of both passive and active compliance. The major additions to the system include the incorporation of series elastic actuators (SEAs) to the arms and torso joints which provide stable torque feedback and thus enable the active control of compliant behavior. They also provide passive compliance to account for finite actuator impulse responses. A distributed control architecture to: support higher-performance brushless motors, make software upgrades easier and more convenient, and improve assembly modularity. And a new drivetrain mechanism that decreases the backlash in the system to improve precision and performance.

The most significant development is the addition of SEAs into the arms and torso joints of the robot. The benefits of SEAs include joint torque measurement, increased passive compliance, and stable torque control [14]. Since the actuators have high inertias and latency associated with real time control, the passive compliance helps reduce effects of large impulses. Due to the constraints of most mobile robots, it is desirable to operate motors from a DC power source. DC motors operate most efficiently at high speed and low torque and therefore large gear reductions must be used. These reductions introduce nonlinearities and friction to the system which make open loop torque control difficult and inaccurate. Torque measurement directly at the joint allows for accurate closed loop torque and/or impedance control to be implemented. This work discusses the development the joint mechanics, the unique sensor arrangement used, a simple impedance controller, and its implementation on a 1 degree-of-freedom (DOF) SEA prototype.

The second major change is the transition to a distributed embedded system. Due to technological advancements, it is now possible to purchase powerful motor controllers that are small enough to locate places outside of the robot torso. In uBot-6, all motor and sensor wires had to go from the arm joints back to the body where the motor controllers were located. The new system utilizes local controllers at each joint. These controllers communicate on a bus architecture to the master which is located in the body of the uBot. As a result, fewer wires run from the arms back to the torso and fewer wires travel across the joints of the robot. Wires crossing joints are generally a common point of failure in robotics, thus reducing these crossings increases the durability and decreases the required maintenance of the robot [15]. The new embedded system also allows for the use of brushless direct current (DC) motors. Commercially available brushless motors have a higher power density than the brushed DC motors used in the uBot-5 and 6, allowing for the uBot-7 to have a higher power density. The testing of this



distributed embedded system on the SEA prototype is explored but the implementation in the robot itself is beyond the scope of this work.

Thirdly, the drive train has been redesigned to decrease the amount of backlash in the mechanism. Currently, planetary gearheads drive a belt mechanism that turn the wheels. The gearhead has  $\sim 1^\circ$  of backlash at its output which results in a dead band in the control when the motor direction changes. This makes the balancing of the robot less stable and more challenging. To alleviate this problem, a new low backlash belt mechanism is implemented that eliminates the need for planetary gearheads.

It is important to understand that there are many hardware approaches to increase the manipulation and safety capabilities of a robot. The choice of incorporating SEAs into the platform does not suggest that this is the best solution to accomplishing this goal but is an approach that has been shown to work in other platforms that will be discussed in SECTION 2.3, *COMPLIANT HUMANOIDS*. Torque feedback can be accomplished in many ways beyond measuring spring deflection and compliance can be added to a system both passively and actively. This work covers the design and implementation of the SEAs but does not exhaustively explore the systems performance as compared to other approaches. As the uBot-7 is an experimental platform, it will provide insight into what a system like this can accomplish.

### 1.3 Thesis Outline

This thesis begins with a discussion of background work. First, the two prior uBot platforms, uBot-5 and 6, are overviewed. It is important to have an understanding of these two platforms because uBot-7 has been designed to build on their capability. Next, the concept of series elastic actuation is discussed and is followed by a discussion of the previous work done in this area. Since the uBot is a humanoid-like platform, other humanoids that use SEAs are reviewed. This background forms the foundation for the development work presented in this thesis.

Next, an overview of the mechanical design is presented in CHAPTER 3, *Mechanical Design of uBot-7*. This includes the mechanism design, an overview of the distributed embedded system, motor-gearhead selection, and spring design. The SEA joints, drivetrain design and spring constant selection will also be discussed in this chapter. Then the sensor design is discussed in CHAPTER 4, *Sensor Design*. Due to the unique requirements of the uBot and SEAs, unique sensors were developed to measure joint position and spring deflection. These sensors are discussed in CHAPTER 4, *Sensor Design*. In the controller design section, a mathematical model of an SEA is derived. Using this model, a torque controller is developed. This torque controller is then used to develop a joint-level impedance controller. To evaluate the mechanical design and control combination, a one degree-of-freedom (DOF) SEA bench-top prototype was fabricated to test the mechanical design, sensor design, control hardware, and control algorithms. The results of this are discussed in Chapter 6, *Implementation and Experiments*, for both a torque and impedance controller. In CHAPTER 7, *Recommendations for Future Implementation*, a list of improvements that can be made to the platform is outlined and CHAPTER 8, *Conclusions*, the contributions of this thesis are outlined.

## CHAPTER 2

### BACKGROUND

#### 2.1 uBot Overview

The uBot is a robot platform that has been developed at the University of Massachusetts' Laboratory of Perceptual Robotics as a high performance-to-cost solution to mobile manipulation focusing on whole body dexterity. The first iterations of the robot (models 0 through 3) were basic, and consisted of a combination of hobby servo motors and printed circuit boards for body structure. Even though these robots were simple, they demonstrated the merit of a dynamic balancer with arms. Researchers began studying what could be accomplished with such a robot and found that this was a unique mobile manipulator that became a means to explore new research avenues. Subsequent iterations of the uBot, such as uBot-5 shown in Figure 2.1, have contributed to the concepts of dexterous mobility [4]–[6], autonomous skill acquisition [7], [8], emergency response [9], and physical rehabilitation [10]–[13].

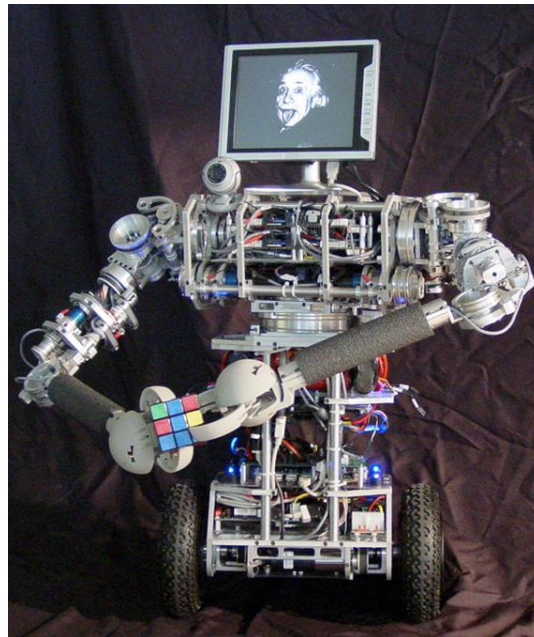


**Figure 2.1** uBot-5 [4]

The robot's form gives it many advantages. It can operate in many of the same environments as biped humanoids which includes environments designed for humans such as hospitals, factories, or households. It was shown that, with its small footprint, high center of mass, and all else equal, it can outperform statically stable mobile manipulators with large bases and low center of masses, like the one shown in Figure 2.2, at pushing tasks such as closing drawers in a household [16]. Since the early uBot versions were used to develop the concept, this thesis only discusses the most advanced versions, uBot-5 and 6, which are the most capable platforms to date.



**Figure 2.2** iRobot's PackBot is a good example of a traditional mobile robot that has a low center of mass and a large footprint [17]

uBot-5 has made the largest contribution to the research community out of all of the uBots to date as it is a highly capable platform that has been operating for over 5 years [4]. The

robot is capable of different postural and mobility modes including balancing, tripod, quadruped, and prone [4]. The balancing capabilities of the uBot-5 design have been proven through disturbances induced by impacts with a boxing glove, a human foot, and even dodge balls [18].

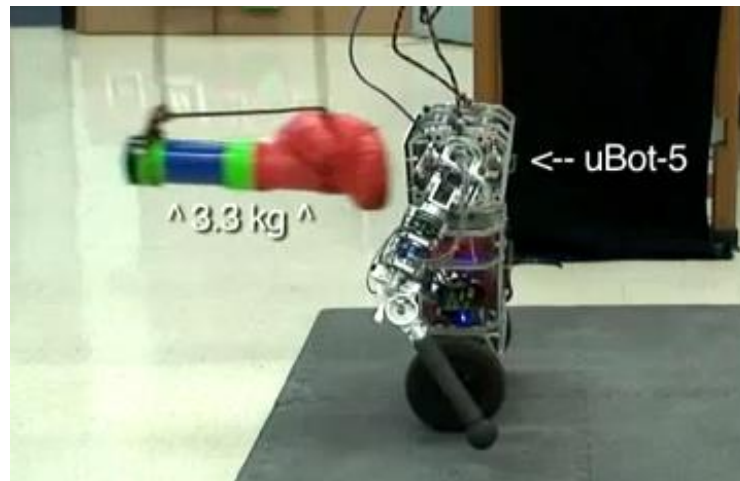


**Figure 2.3** uBot-5 learning dynamic arm motions for postural recovery [18]

The frame is mainly composed of parts fabricated from 6061 aluminum which is a relatively strong, lightweight, and inexpensive material. Its design allows most parts to be easily replaced upon failure or modified as necessary, key aspects of a research prototype. The design also leverages commercial components (motors, gearheads, etc.) that can be purchased from reliable manufacturer's existing product lines thus reducing cost, lead times, and availability of replacement parts. This contributes to the overarching theme of the uBot: a modular, robust, and, relative to other comparably capable platforms, inexpensive research platform.

**Table 2.1** uBot-5 actuator peak torques, no load speeds, and mechanisms

Joint	Torque (Nm)	No Load Speed (rpm)	Mechanism	Reduction:1
Shoulder Flexion	2.7	77.0	Planetary Gearhead + Cable Drive	86
Shoulder Abduction	2.6	73.7	Planetary Gearhead	116
Shoulder Twist	1.0	199.0	Planetary Gearhead	43
Elbow Flexion	1.0	199.0	Planetary Gearhead + Cable Drive	43
Torso	4.1	50.2	Planetary Gearhead + Cable Drive	132
Wheels	0.5	473.1	Planetary Gearhead + Belt Drive	14

**Table 2.2** uBot-6 actuator peak torques, no load speeds, and mechanisms

Joint	Torque (Nm)	No Load Speed (rpm)	Mechanism	Reduction:1
Shoulder Flexion	16.9	20.7	Planetary Gearhead + Cable Drive	318
Shoulder Abduction	8.5	41.4	Planetary Gearhead	159
Shoulder Twist	8.5	41.4	Planetary Gearhead	159
Elbow Flexion	8.5	41.4	Planetary Gearhead + Cable Drive	159
Torso	7.0	49.8	Planetary Gearhead + Cable Drive	132
Wheels	5.7	137.9	Planetary Gearhead + Belt Drive	43

**Figure 2.4** uBot-6 in knuckle walking mobility mode

uBot 5's capability for multiple mobility modes was proven to be useful, and thus the uBot-6 was developed to improve upon these capabilities. In order for the uBot-5 to complete a push-up or knuckle walking task its motors were pushed close to their operational limit and therefore higher torque actuators were used in uBot-6. The actuator specifications of uBot-5 and 6 can be seen in Table 2.1 and Table 2.2 respectively. Figure 2.4 shows the uBot-6 knuckle

walking. The uBot-6 also incorporated wheels on its elbows which can be placed on the ground and enable the additional mobility mode of prone scooting. This mobility mode is a faster way to travel than balancing. The importance of this mode was also exemplified in [5] where the robot navigates under a low table by prone scooting to reach an area that was otherwise unreachable. The mobility modes that the uBot-6 is capable of are depicted in Figure 2.5.

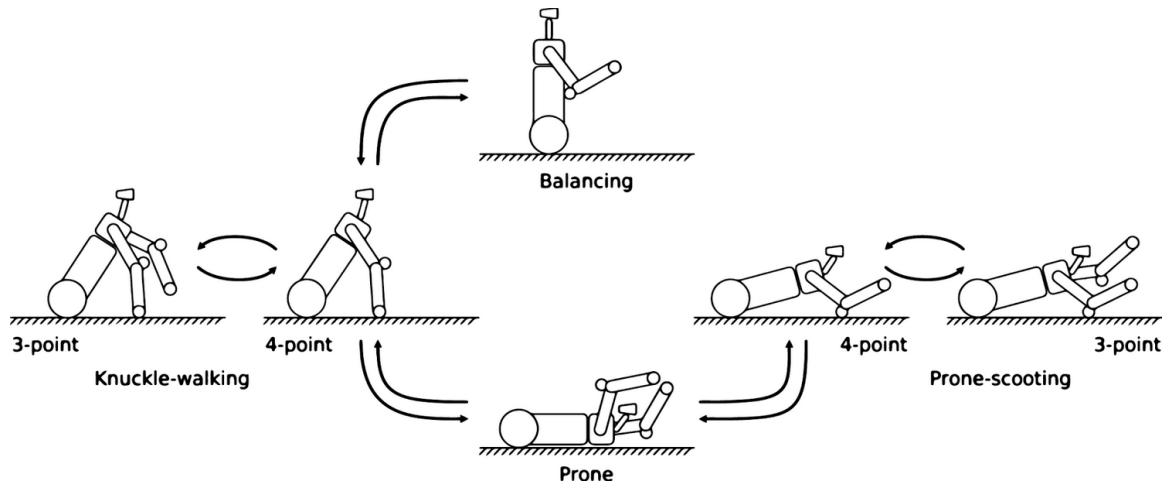


**Figure 2.5** The different postural modes uBot-6 can attain to accomplish a goal [5]

It can be seen that uBot-6 has more torque in all of its joints than the uBot-5, but has lower no load speeds. No load speed has not been a limiting factor in the uBot yet because the manipulation tasks that are desired for the platform to complete do not require high speeds. This was an important realization as it helped determine the actuator specifications for uBot-7.

It is also important to note that the motors used in uBot-5 and 6 were driven by MOSFET H-Bridges that were capable of supplying up to three amps to each arm and torso motor, and six amps to the wheel motors. The motors can be driven at higher peak torques intermittently and thus the current limitations of the H-Bridge make it the torque limiting component. Because of this, the uBot-7 uses new electronics enabling use of the whole torque range of the actuators.

The peak load rating for the gearheads in uBot-6 is 6 Nm [19]. As seen in Table 2.2, the uBot-6 operates outside of this region. This has not yet caused a problem but may eventually result in premature failure of the gears.

**Table 2.3** uBot-5 & 6 weight and dimensions

		uBot-5	uBot-6
Body	Height (mm)	605	710
	Shoulder Width (mm)	575	603
	Base Width (mm)	400	405
	Weight (kg)	19.5	24.3
Arms	Shoulder Link Length (mm)	110	112
	Upper Arm Link Length (mm)	254	330
	Forearm Link Length (mm)	236	365

The uBot-6 is also slightly bigger than the uBot-5. Table 2.3 shows the dimensions of both uBot-5 and 6 with simple ball end-effectors and no neck or vision system. The larger size gives uBot-6 some advantages over uBot-5 such as a larger reach and work envelope. It also provides space for more computing hardware, batteries, and higher power motors. The size has some disadvantages though such as increased forces generated during falls. The uBot-7 was designed to be close to the same size as uBot -6. Understanding the specifications of the previous platforms helps to form the basis for developing the uBot-7.



## 2.2 Series Elastic Actuation (SEA)

There are a number of mechanical design approaches that can be taken to prevent high forces in the case of a collision between a mechanism and its environment. These include shear pins, clutches, covering it in a compliant material, or active force control. One specific approach to this problem is the addition of passive compliance between the motor and the link of a robotic joint. This approach is known as series elastic actuation (SEA) [14] and is popular in the field of robotics due to its benefits. A general schematic of a SEA can be seen in Figure 2.6 which includes the motor, spring, and output link. Motor inertia, motor torque, motor position, and motor damping are represented as  $J_m$ ,  $T_m$ ,  $\theta_m$ , and  $D_m$  respectively. The spring constant and spring deflection are represented as  $K_s$  and  $\theta_s$  respectively. And external torque applied to the actuator, the link damping, and the link position are represented as  $T_i$ ,  $D_L$ , and  $\theta_L$  respectively. The motor and gearhead are assumed to be one mass with effective inertia  $J_m$ .

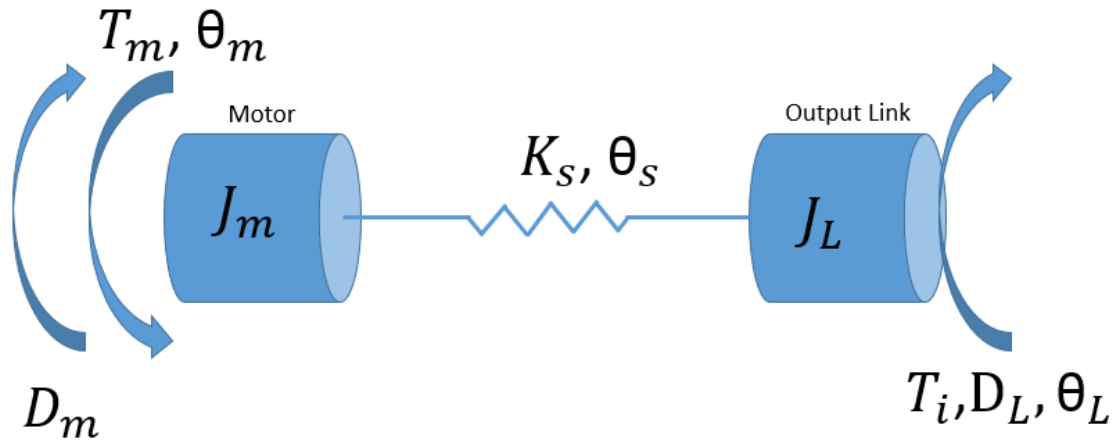


**Figure 2.6** Schematic of series elastic actuator

The compliance lowers shock loads. This is especially important in mobile robotic applications where the actuators are typically DC motors as they offer a compact, power dense package as compared to pneumatics and hydraulics. Since DC motors operate most efficiently at relatively high speeds and low torques, it is necessary to either vastly oversize the motor or use

a mechanical reduction to increase the torque of the actuator. Typically, a motor and gearhead is the more compact, torque dense, option making it more desirable for mobile applications. The reduction has the effect of increasing the effective motor inertia at the gearhead output by a factor of the reduction ( $N$ ) squared. As an example, the uBot-7 elbow has a 159:1 reduction, and thus the motor inertia is increased by a factor of 25,281 resulting in an effective inertia of 458  $\text{gm}^2$ . The forearm link of the robot only has an inertia of 33  $\text{gm}^2$  and thus it can be seen that the effective motor inertia dominates the kinetic energy to be absorbed upon impact.

The second major benefit of SEAs is that the deflection of the compliant element can be measured and joint torque can be calculated based on this deflection. Torque feedback allows the implementation of a closed loop impedance controller at each joint. Due to the nonlinearities and friction present in mechanical transmissions, modeling the system accurately is difficult and thus open loop torque control (or closed loop current control) will not be accurate. Since the deflection is measured after the gearhead, this closed loop control is far superior in this situation. The local impedance controllers can effectively operate even if contact is made in locations other than the end effector which is not the case if force is only measured at the end effector. This is especially important in the case of the uBot as it purposefully operates in these scenarios. Prone scooting is a good example of this. It is also important to note that if torque is measured, it can be accurately controlled with a stiff joint, but the latency associated with a real time system with finite actuator responses creates the desire to have some sort of passive compliance in the system.

SEAs can also be used to increase the manipulation capability of the robot through the use of force feedback. It has been shown that stable and accurate torque control can be implemented even at low controller frequencies with SEAs [20]. As discussed in [3], pure manipulation occurs when an object is completely known. Pure exploration occurs when the

object is fixtured and not known. Dexterous manipulation is a combination of exploration and manipulation and can be thought of as an object centered manipulation in which multiple manipulators are in contact with the object. The object's desired motion can be used to determine the forces that the manipulators apply to that object. Because of this, incorporating joint torque feedback can be used to increase the dexterous manipulation capability of the robot. The passive compliance in the SEA will also reduce the large forces that correspond to small positioning errors during multiple armed manipulations thus making this type of manipulation require less precise positioning.

As discussed above, SEAs have many benefits, however, as compared to rigid actuators but they also have drawbacks and it is important to understand these drawbacks when using SEAs. The addition of compliance to the system changes the dynamics of the system in a way that lowers the position control bandwidth. It also has a tendency to lower the positioning accuracy of the system, however, the implementation of SEAs in uBot-7 attempt to minimize this problem. For certain applications, large position control bandwidth and positioning accuracy is not necessary and adequate performance can be obtained with SEAs. Inherently, a system like this requires the addition of mechanical components and sensors. This has a tendency to raise the cost of the robot as well increase the number of potential failure points.

Currently there have been many SEAs designed and tested. For most robotic applications it is desirable to operate at relatively high torques and low speeds. It is also desirable to maintain a lightweight actuator because actuators may be placed at distal joints where they have large effects on the system's inertia. In mobile applications, it is desirable to operate the system using a DC power source to avoid additional control hardware or hydraulic/pneumatic tanks. Working within these design constraints most SEA designs have used DC motors with large gear reductions. These gear reductions introduce control challenges

due to the friction, backlash, and torque ripple [20]. To minimize these effects, SEAs have been developed that use frameless DC motors coupled with low backlash mechanics such as harmonic drive gearheads [15], [21]–[24] or ball screws [25], [26]. These approaches use expensive hardware and highly custom components. Other SEA designs have shown that less expensive components such as planetary gearheads can be used and can attain torque control bandwidths acceptable for use on the uBot [20], [27]–[31]. This is important because it means planetary gearheads can be used in the uBot and thus that is what is covered in this thesis.

Due to the nature of the uBot’s functionality, it has unique needs for its actuators. The actuators must be capable of both manipulation of objects and attaining the mobility modes outlined in Figure 2.5. It must also maintain a relatively low price which excludes the use of harmonic drive gearheads. Chapter 3 discusses how the SEAs were implemented on the uBot under these constraints.

### 2.3 Compliant Humanoids

Before discussing the design the new uBot-7 platform, it is important to review similar existing robots. Robonaut 2, and COMAN are state of the art humanoid robots that use SEAs. It is important to discuss the designs of these SEAs and their relevance to the uBot-7 development as they have motivated this work.



**Figure 2.7** Rethink Robotics' Baxter™[32]

Before a detailed discussion of Robonaut 2 and COMAN an overview of a different robot is beneficial. Baxter™, by Rethink Robotics, and is shown in Figure 2.7. Baxter was introduced to the robotics community in September 2012 [32]. Baxter is commercially available and can be used as an industrial robot on the factory floor (although it is also being used by many research institutions). It has a long list of features that include intuitive user interface, multiple end effectors, and, most notably, a base price of \$22,000 when first released. Unlike most industrial robots that are required to operate at a safe distance from any person or even in a cage, Baxter is designed to work next to a human safely. The reason this robot is worth noting in this thesis is

because these features are made possible by the SEAs that it uses. These actuators help reduce the chances of a dangerous collision between Baxter and a human or the environment. They also allow for less expensive actuators to be used while maintaining stable force control.

Rethink Robotics has shown, through the production of Baxter™, that it is possible to make a 14 DOF robot that uses SEAs and force feedback at a low price point. Excluding the wheels, the uBot is a 9 DOF robot that strives to maintain a similar cost.

### 2.3.1 Robonaut 2

Robonaut 2, shown in Figure 2.8, is a humanoid robot developed by NASA and General Motors and is one of the most advanced systems of its type to date [15,33]. The robot resembles, and is scaled to, a human body from the waist up. The purpose of Robonaut 2 is to explore capabilities of a humanoid robot outside of the Earth's atmosphere [11]. Since this is a dangerous and expensive place to send humans, work is being done to explore what maintenance tasks can be done by the robot. Currently, a Robonaut 2 is on the International Space Station. The paper published about Robonaut 2's hardware, [15], gives an overview of the robot and that is what this section discusses.



**Figure 2.8** NASA's Robonaut 2 [15]

Robonaut 2 is an improved version of the first Robonaut which is a more traditional platform that does not have compliant joints. The new robot has many improvements to the electromechanical design, sensing integration, control strategy, and user interface. This has led to increased speed, strength, dexterity, and human interaction capability [15].

One of the most notable improvements is the addition of SEAs in the arm joints of the robot. These actuators consist of brushless DC motors coupled to harmonic drive gear reductions. They also take advantage of brakes to minimize power consumption. The output of the gearhead is connected to a torsional spring with a linear spring constant. These springs have a unique 2-dimensional design shown in Figure 2.9 and can thus be made with inexpensive manufacturing techniques. This geometry allows for a relatively thin material to be used and the combination leads to a very compact SEA package size. The spring constants are designed to the actuator such that the max continuous motor output torque corresponds to maximum deflection thus making torque measurable over the full continuous range of the actuator's torque.



**Figure 2.9** Springs used in Robonaut 2's SEAs [15]

To measure position, each of the joints incorporates two absolute angular position sensors that measure motor position and SEA output position. The spring deflection can be found from the difference of these two measurements. Since the harmonic drive gearheads have low backlash, this measurement can be used to accurately calculate joint torque.



Since the uBot's design goal is a high performance-to-price solution, harmonic drive gearheads, frameless motors, and 19-bit position sensors would put the robot out of the desired price range. The spring design that the Robonaut 2 uses have a planar design that results in a lightweight package that is easy to manufacture. Because of this, similar springs are used in the uBot-7 SEAs. The uBot design will also leverage the way in which the Robonaut 2's spring constants were designed to the continuous torque of the actuator.

### 2.3.2 COMAN



**Figure 2.10** Compliant HuMANoid Platform from IIT [34]

Compliant HuMANoid Platform, or COMAN, shown in Figure 2.10, is a robot that is being developed in the Italian Institute of Technology's Advanced Robotics group. This robot is the predecessor of iCub, the child humanoid robot and cCub, the compliant version of iCub. As such, the actuator design of COMAN came directly from cCub. Similar to the Robonaut, COMAN uses frameless brushless DC motors. The frameless motors allow the design of the motor frame to be part of the support structure which creates a very compact and integrated package. This requires highly custom components and thus raises the cost and decreases the modularity of the platform. The motor is coupled to a harmonic drive gearhead with a 100:1 reduction [21].

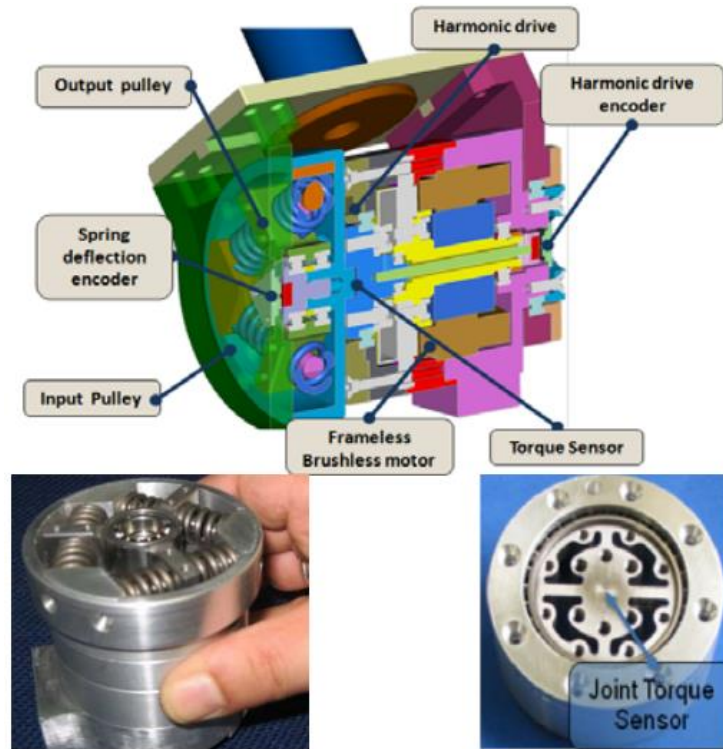


**Figure 2.11** COMAN's series elastic actuators featuring a custom spring design, and torque load cell [22]

The compliance of the actuator is attained with a novel arrangement of linear springs and is capable of a maximum deflection of  $\pm 0.18$  radians ( $\pm 10.3^\circ$ ). This spring, a cross-sectional view of the actuator, and the torque load cell can be seen in Figure 2.11. Notice that the actuator includes three position sensors: an optical encoder measuring spring deflection, a 12-bit absolute magnetic encoder measuring the harmonic drive position (input to the spring), and a 12-bit absolute magnetic encoder measuring the link position (spring output). A custom semiconductor based torque load cell also measures actuator torque [22]. The actuators are capable of peak torques ranging from 20 Nm to 40 Nm. This robot has been useful to study spring parameter and stiffness tuning through resonant frequency excitation, stabilization of bipedal robots, and bipedal walking with compliant actuators [34]–[42].

The actuators used in COMAN have high quality mechanics that result in low backlash and a large range of spring deflections. The large deflection range deviates further from a position controlled robot and therefore may require more development to implement on the uBot, however, this is an area that can be explored further once the platform is completed. The springs in this case are also bigger and heavier than the ones used in Robonaut 2.

COMAN measures all joint states which include: motor position, spring deflection, output link position, and torque. This is beneficial for control as these states are well known and can be used to implement higher performing controllers. They also allow for calibration to be done more easily. Spring position and torque measurement from the load cell can be cross referenced for calibration as well as combinations of motor position, spring deflection, and output link position. This would be an ideal design for the uBot, however, the torque load cell and motor gearhead combination is cost prohibitive for the application.

## CHAPTER 3

### MECHANICAL DESIGN OF UBOT-7

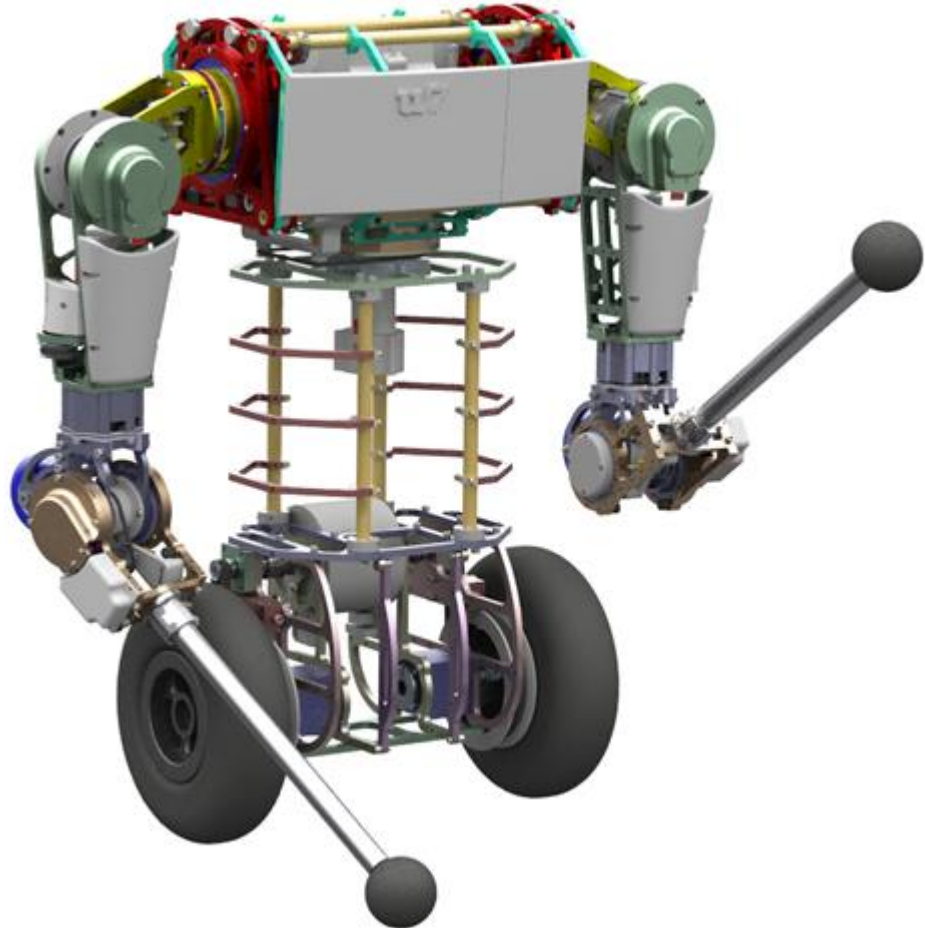


**Figure 3.1** Rendering of the uBot-7 CAD model

The uBot has been designed as a high performance-to-price solution to mobile manipulation and whole body control. This mission forms the basis for the specifications to which the robot was designed. This chapter starts with an overview of the design requirements, which is followed by a description of the SEA mechanism designed for uBot-7. Next, a description of the motor-gearhead combinations and spring design for the SEAs is discussed. The selection of spring constants for each joint is then covered and this is followed by an overview of the arm and all of its joint designs. Next, the new drivetrain mechanism is then shown. An

overview of the embedded system is provided and the chapter concludes with a summary of the design.

### **3.1 Design Requirements**

The requirements for uBot-7 were developed based on experience using the previous platforms and functional requirements developed based on tasks uBot-7 is expected to perform. The prior platforms have proven to be very functional. However with increased use, new functions were desired that require increased capability. To increase the capability it was desirable to add torque feedback, passive compliance, and active compliance. SEAs were selected as they can be used to provide all of these. This forms the first requirement: SEAs in all joints but wheels.

The functional requirements were based on expected manipulator actions and include moving the shoulder flexion joint through  $180^\circ$  in three seconds, and moving all other joints through the same range in one second. This motion can be seen in Figure 3.2. The uBot must also be able to hold 10 N statically in the two configurations shown in Figure 3.4. Note that in this scenario the robot would have to lean back to statically maintain this position. Similar to the uBot-5 and 6, uBot-7 must be capable of completing a push up under its own power as shown in Figure 3.3. These scenarios can be used to determine the required minimum actuator specifications, however the pushup requirement needs knowledge of the completed system. As a starting point in the design process, the uBot-7 was assumed to weigh the same as uBot-6. Since uBot-6 could adequately do a push-up while operating in the continuous range of the actuator the uBot-7 torques were determined to be a minimum of equal to uBot-6. It is important to note, however, that the uBot-6 torso joint was weaker than the other joints and would benefit from more torque. A factor of 1.5 was chosen to be the minimum amount to

increase this. An outline of the torques and speeds derived from these functional requirements can be seen in Table 3.1.

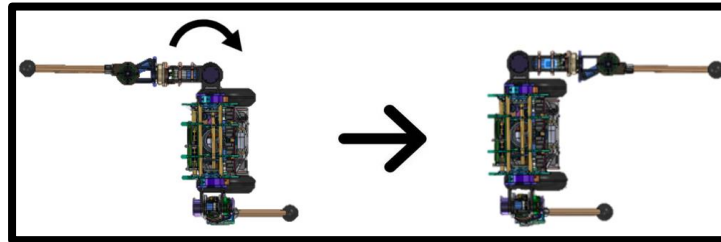


**Figure 3.2** uBot moving shoulder abduction joint 180°

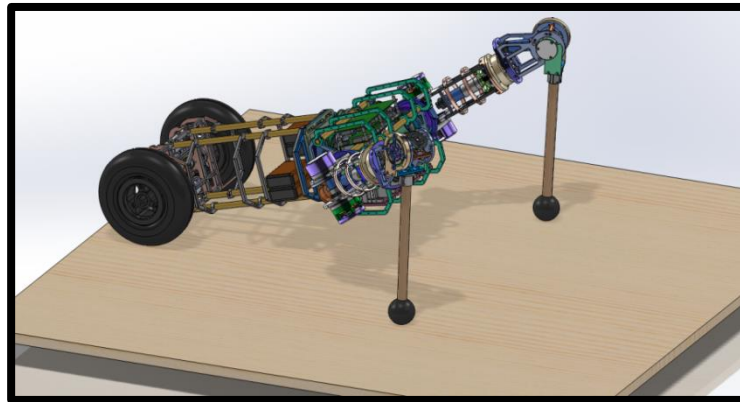


**Figure 3.3** uBot doing a pushup

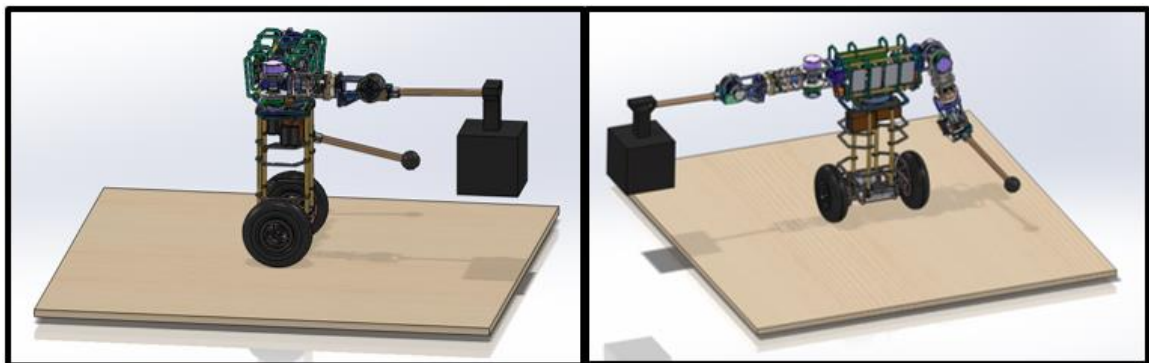


**Figure 3.4** uBot holding a weight in multiple configurations

The next requirement of the uBot has to do with the size and weight of the robot. The uBot-7 robot should be about the same size as uBot-6. At a minimum, it can be no smaller than uBot-5 and, at a maximum, only slightly larger than uBot-6. Even with the addition of components and stronger motors, the weight of the uBot must not far exceed that of uBot-6.

This is driven by the desire to keep the platform inexpensive and safe. With increased size, more material and higher power actuators must be used. This increases weight and therefore the robot can cause more damage in the case of a fall.

The spring parameters for each joint were not specified directly for this project as it is an area that needs to be explored further to determine what makes the spring optimal for the given system. It is also important to note that the platform must be capable of all the mobility modes of uBot-6 that are shown in Figure 2.6. A summary of requirements for the uBot-7 can be seen below:

**Table 3.1** uBot-7 Design Requirements

Size	Height (mm)	605-750	Range
	Shoulder Width (mm)	575-650	Range
	Base Width (mm)	400-415	Range
Weight	Weight (kg)	30	Max
Joint Torque	Torso (Nm)	12.3	Min
	Shoulder Flexion (Nm)	16.9	Min
	Shoulder Abduction (Nm)	11.2	Min
	Shoulder Twist (Nm)	8.5	Min
	Elbow Flexion (Nm)	8.5	Min
Joint Speed	Torso (rpm)	30	Min
	Shoulder Flexion (rpm)	10	Min
	Shoulder Abduction (rpm)	30	Min
	Shoulder Twist (rpm)	30	Min
	Elbow Flexion (rpm)	30	Min
Range of Motion	Torso (°)	360	$\pm 10^\circ$
	Shoulder Flexion (°)	720	$\pm 10^\circ$
	Shoulder Abduction (°)	270	$\pm 10^\circ$
	Shoulder Twist (°)	360	$\pm 10^\circ$
	Elbow Flexion (°)	120	$\pm 10^\circ$

Before finishing the discussion of design requirements it is important to understand that the robot is a research platform and the full set of tasks and capabilities



of the platform remain to be explored. Because of this, the uBot-7 design is intended to meet or exceed the specifications in or order to maximize the platform's capability.

### 3.2 SEA Mechanism Overview

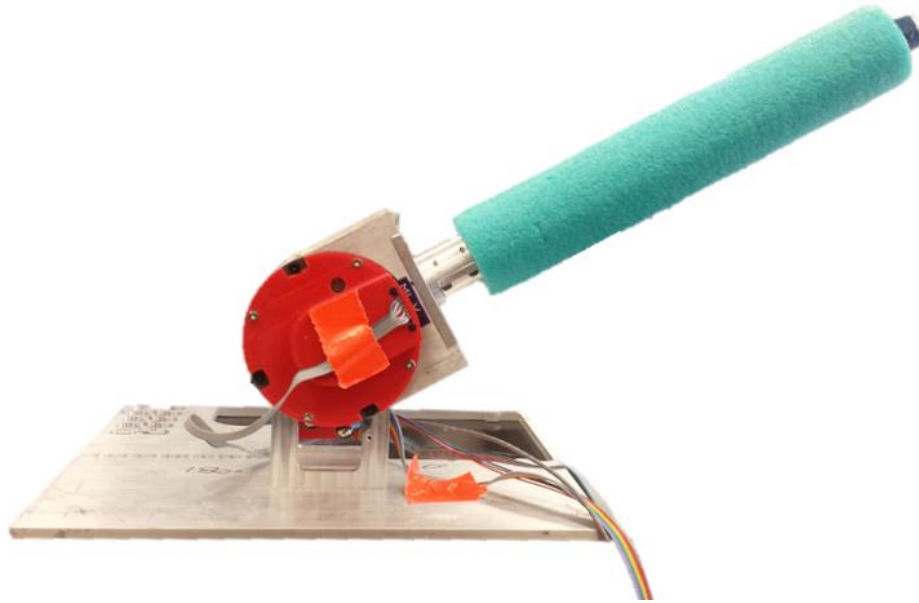


**Figure 3.5** Prototype SEA developed for design validation

SEAs consist of a motor that is coupled to a link via a compliant element as the schematic depicts in Figure 2.6. The uBot concept has been developed as a relatively low cost solution and, due to its low production quantities, uses relatively inexpensive commercial components. Extending this to the motors gearhead combination, brushless out runner DC motors and planetary gearheads were used. These components were sourced from commercially available components to reduce cost and increase modularity. For the compliant element, a torsional spring with a linear spring constant is used. This spring has a 2-dimensional geometry and therefore can be fabricated from planar cutting techniques such as water jet cutting. All of the uBot-7 actuators were designed to have the same fundamental mechanics and only differ in size, shape, torque, and speed. A prototype SEA was fabricated to validate the design and this model will be used to explain the design throughout this section. The finished SEA prototype can be seen in Figure 3.5. The size and torque specifications were developed to

allow higher torques in proximal joints and lower weight in distal joints. The selection process is further discussed in Section 3.3.

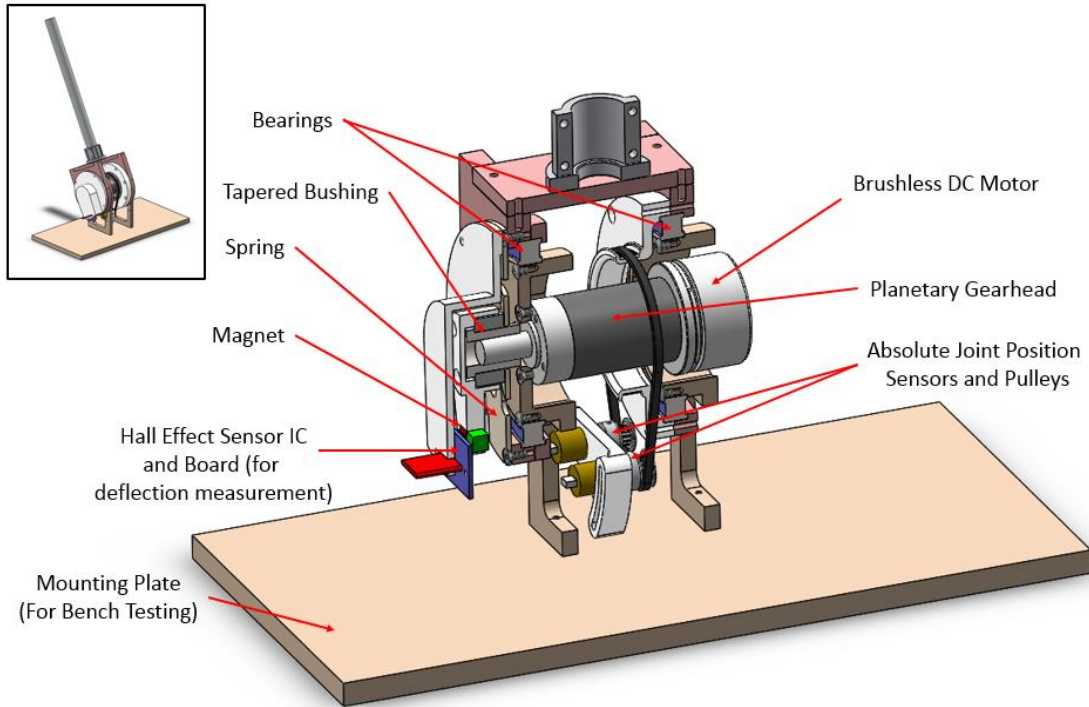


**Figure 3.6** Cross-section of prototype SEA joint for uBot-7

A cross-sectional view of the bench top SEA prototype can be seen in Figure 3.6. Notice the brushless DC motor and the planetary gearhead. These form the  $J_m$  component shown in the schematic in Figure 2.6. The output shaft of the gearhead is connected to the torsional spring with a tapered bushing. This was found to be a robust solution to connecting the motor shaft to the spring as the tapered bushings are rated for the joint load and have zero backlash. As previously stated, the spring features a planar design. This design can be seen in Figure 3.7. The spring arms use the same geometry as NASA's Robonaut 2 [16,45]. Notice that the inner bolt circle connects to the gearhead output shaft and the outer bolt circle connects to the output of the joint. The joint output is supported by two ball bearings labeled above.

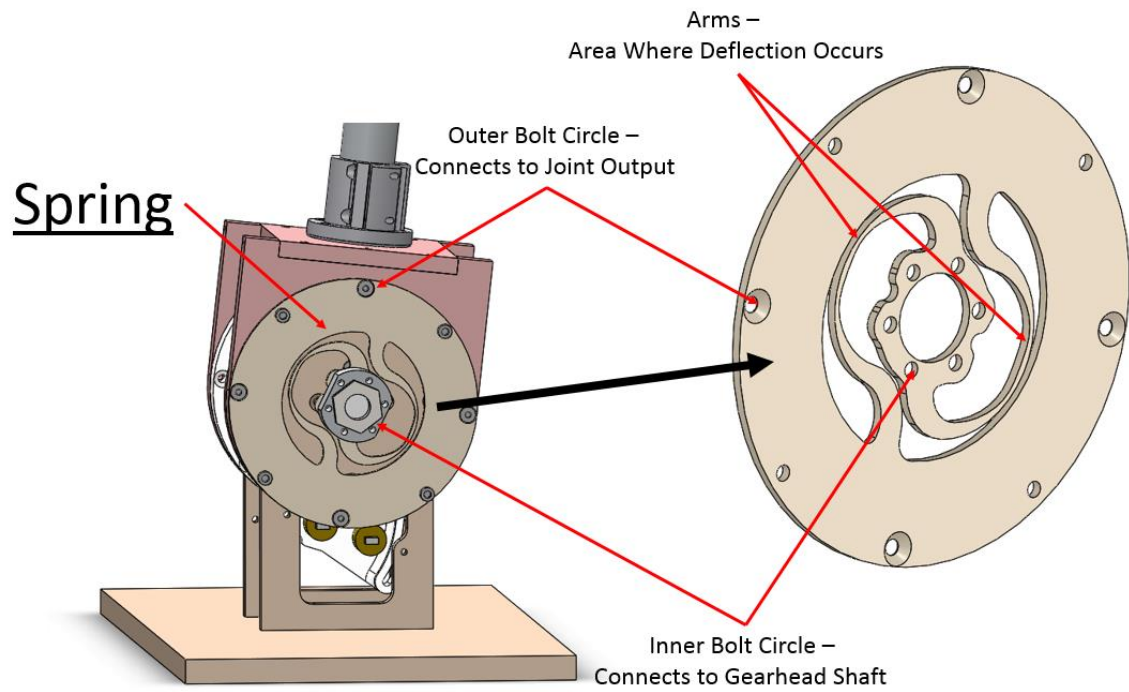


**Figure 3.7** SEA prototype without deflection sensor or cover to show spring used

### 3.3 Selection of DC Motors and Gearheads

The selection of the uBot-7 motor and gearhead combinations were based on the requirements previously discussed. The planetary gearheads used in uBot-6 have about  $1^\circ$  of backlash which lowers the system performance. Higher performing reductions with less backlash are available but are much more expensive. Through use of the platforms, it has been shown that the backlash, back drivability, and robustness of the uBot-5 and 6's planetary gearheads were all adequate for the uBot to complete many tasks. Since the uBot-7 will operate with force feedback this does not directly provide enough evidence to say that planetary gearheads will work in its SEAs. However, it was also shown that planetary gearheads can be used in SEAs to attain torque bandwidths of  $\sim 40$  rad/sec [31]. Based on this, a prototype actuator (shown in Figure 3.5) was constructed that proved the planetary gearheads could attain torque control bandwidths of at least 25 rad/sec. The results of testing this actuator are discussed in CHAPTER 6. Based on this reasoning, similar gearheads to those used in uBot-6 were chosen to be used in uBot-7.

Based on the functional requirements and the performance of uBot-5 and 6 it was determined that all of the joint speeds were adequate to meet desired performance specifications when performing manipulations but the uBot would benefit from higher torques at the proximal joints. Based on these details, the uBot-7 actuators were selected. The motor gearhead combinations were chosen such that the maximum continuous torque of the motor corresponds to the maximum intermittent torque of the gearhead to ensure safe motor operation. This means that the gearhead intermittent torque rating is the torque limiting factor in the actuator and current limitations must be implemented in software to enforce this. Table 3.2 shows the requirements of the joints as well as their actual maximum torque and no load speed. The motors and gearheads used are also shown in this table.

**Table 3.2** uBot-7 joint maximum torque and no load speed compared to the values determined from functional requirements

	Functional Requirements		uBot-7			
	Torque (Nm)	No Load Speed (rpm)	Torque (Nm)	No Load Speed (rpm)	Motor (power)	Planetary Gearhead (reduction)
Torso	12	30	12	39	Maxon EC 45 Flat (70 watt)	Maxon GP 32 HP (159:1)
Shoulder Flexion	17	10	45	19	Maxon EC 90 Flat (90 watt)	Maxon GP 52 C (113:1)
Shoulder Abduction	11	30	21	27	Maxon EC 45 Flat (70 watt)	Maxon GP 42 C (230:1)
Shoulder Twist	9	30	12	39	Maxon EC 45 Flat (70 watt)	Maxon GP 32 HP (159:1)
Elbow	9	30	12	39	Maxon EC 45 Flat (70 watt)	Maxon GP 32 HP (159:1)

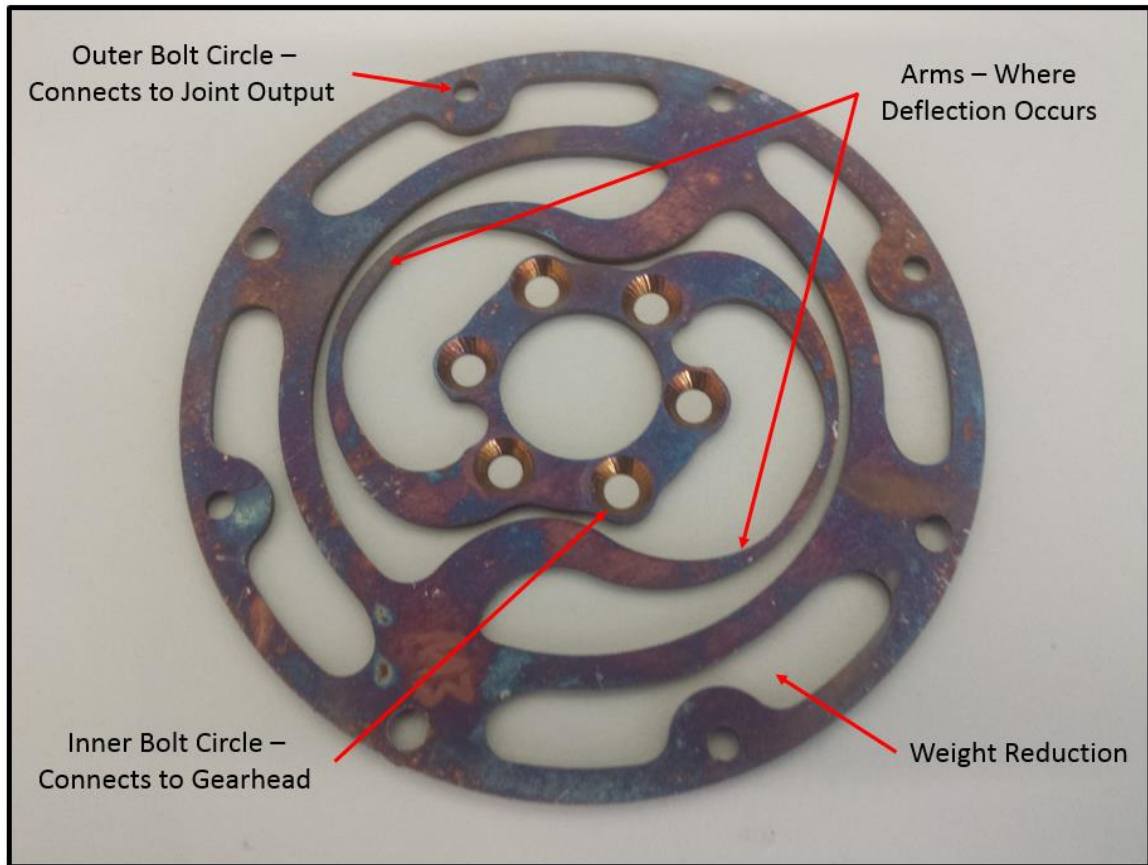
Notice that the torque and speeds requirements are all close to the actual joint specifications with the exception of the shoulder flexion joint. Since this joint is the most proximal, it does not move with the arm. This means that increasing the actuator weight at this location does not increase the moment of inertia of the arm. Since the uBot is a research platform, it was decided that over sizing the motor does not hurt performance and may prove to be beneficial in future applications. These motors do however weigh more than the distal motors and add a total of 1.2 kg to each arm. If future exploration shows that these motors are over powered this would be a good area to reduce weight.

Table 3.3 shows the torques at which the uBot-6 and uBot-7 operate. It is important to note that the torques in uBot-6 are 40% over the load rating of the gearhead manufacturers rated torque of 6 Nm (12 Nm in the shoulder flexion) but have not yet caused problems in the platform. The uBot-7 torques are all within the manufacturers ratings. The torques shown in red were increased by over a factor of 2 and the torques shown in yellow were increased by a smaller factor.

**Table 3.3** uBot-6 and uBot-7 joint torque and speed specifications. The red boxes indicated the a change of over a factor of 2, the yellow boxes indicate a smaller change, and the green boxes indicate the value is approximately the same

	uBot 6		uBot 7	
	Torque (Nm)	Speed (rpm)	Torque (Nm)	Speed (rpm)
Torso	8.2	45	12	39
Shoulder Flexion	16.9	21	45	19
Shoulder Abduction	8.5	41	21	27
Shoulder Twist	8.5	41	12	39
Elbow	8.5	41	12	39

### 3.4 Spring Design



**Figure 3.8** Spring geometry used in uBot-7. [16,45]. The discoloration is a result of the heat treatment process

The springs in uBot-7 use the same arm geometry as the Robonaut 2 [16,45]. This can be seen in Figure 3.8 where the inner bolt circle is used to connect to the gearhead and the outer bolt circle connects to the output of the joint. The material used for this spring was 17-4PH H900 which has a relatively high yield strain, about 4 times that of a 1018 mild steel [44]. This material was also easily available through commercial suppliers in sheet stock and low quantities which helps lower the material cost and manufacturing processes. The discoloration of the metal in this picture was due to the heat treatment process.

To design the spring specifically for each joint, the spring constant needed to be changed. Through finite element analysis, it was found that the spring constant of this spring



can be changed with material thickness. It was also found that there was a linear relation between spring constant and material thickness as can be seen in Figure 3.9. This is intuitive because it would be expected that the spring constant would double if two springs were used which is effectively doubling the thickness. Because of this, springs can be designed to the desired spring constant easily. The choice of a proper spring constant is a more difficult problem and will be discussed in the following section, *Selection of Spring Constants*.

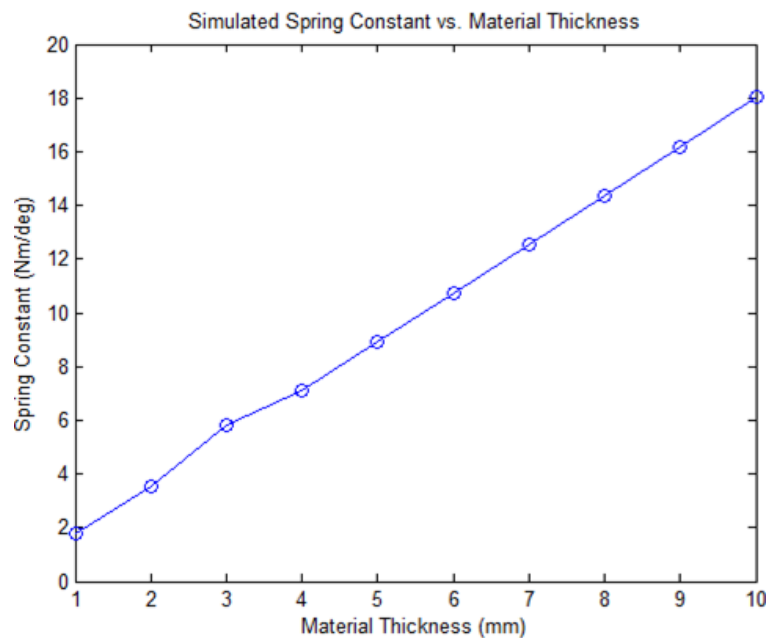


**Figure 3.9** Spring constant from FEA simulation vs. material thickness

### 3.5 Selection of Spring Constants

The spring constant affects the dynamics of the system, torque sensing range and resolution if measured with a position sensor, and the safe speed at which the system can operate and thus the choice of a proper spring constant is a critical decision when designing a SEA. Methods of correlating the passive compliance to the systems safe operating speeds were discussed in [45], however, this method is not directly applicable to the uBot because the platform is not guaranteed to maintain a certain speed of operation in the case of a fall. Other methods of optimizing the stiffness parameters were explored using COMAN that focused on the resonant frequencies of the system [38, 42]. Choosing the optimal spring constant for an SEA is an area that still has much room for study and is largely system and application dependent.

For the uBot-7 design, the spring constant selection method used for Robonaut 2 was used. The springs were designed such that the maximum deflection of the spring occurs at the maximum torque of the motor. This was done so the torque sensing range of the joint corresponds to the actuators output torque range. This allows closed loop torque control to be implemented over the full range of actuator torques. Neglecting friction and assuming the output of the actuator to be locked, the natural frequency of the system can be seen in the below equation:

$$\omega_n = \sqrt{k_s / J_m} \quad (3.1)$$

where  $k_s$  is the spring constant and  $J_m$  is the motor inertia after the gearhead as seen from the input to the spring. It can be seen from this equation that increasing the spring constant raises the natural frequency of the system. As shown in [46], increasing the natural frequency of the system increases the open loop torque control bandwidth of that system. This, however, comes at the cost of the spring deflection sensor resolution. Other SEA designs have maximum spring deflections that range from 3° to 10°[21, 29]. To obtain an adequate amount of torque sensing

resolution and passive compliance while maintaining a sufficiently high stiffness, the maximum deflection range of the spring was chosen to be  $\pm 4^\circ$ . Since the uBot-7 is a research platform, future investigation will prove if this spring deflection range is acceptable and further work should be put into optimizing this parameter. Because of this the system has been designed such that the spring constant can be changed simply by replacing the spring. The experimental results of choosing this spring constant are discussed in CHAPTER 6, *Implementation and Experiments*.

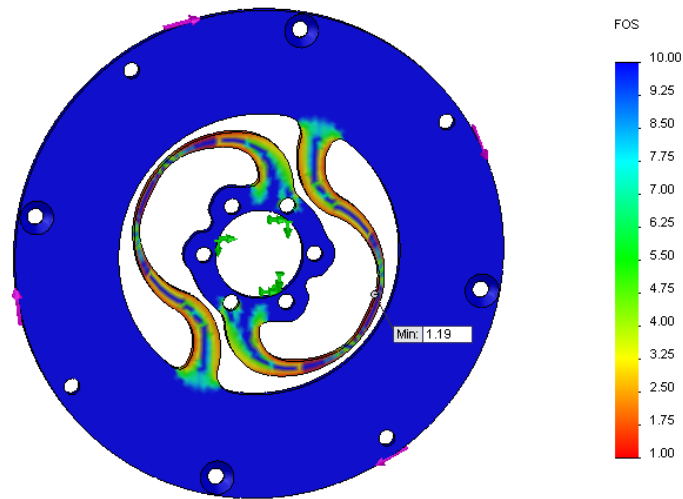


**Figure 3.10** Factor of safety plot from FEA simulation of SEA prototype spring at  $4^\circ$  of deflection

As previously stated, the spring geometry was chosen to be identical to that of Robonaut 2 which utilizes a planar design [15,43]. It was found, through finite element analysis, that with a planar spring design the spring constant varies linearly with material thickness assuming the material is thick enough to avoid buckling. The material used was 17-4PH H900 which was chosen due to its high strain at yield property. Using this material, a finite element analysis (FEA) simulation it was shown that the spring can safely deflect the desired amount of  $\pm 4^\circ$  before yield and has a factor of safety of 1.19. This can be seen in Figure 3.10. The spring constants for each joint can be seen in Table 3.4.

**Table 3.4** uBot-7 actuators peak torques, no-load speeds, spring constants, and motor-gearhead combinations

	Torque (Nm)	No Load Speed (rpm)	Spring Constant (Nm/deg)	Motor (power)	Planetary Gearhead (reduction)
Torso	12	39	3	Maxon EC 45 Flat (70 watt)	Maxon GP 32 HP (159:1)
Shoulder Extension	45	19	11.25	Maxon EC 90 Flat (90 watt)	Maxon GP 52 C (113:1)
Shoulder Abduction	21	27	5.25	Maxon EC 45 Flat (70 watt)	Maxon GP 42 C (230:1)
Shoulder Twist	12	39	3	Maxon EC 45 Flat (70 watt)	Maxon GP 32 HP (159:1)
Elbow	12	39	3	Maxon EC 45 Flat (70 watt)	Maxon GP 32 HP (159:1)

Using equation 3.1 and assuming the output of the joint is locked, the natural frequency for each joint can be calculated. This can be seen in Table 3.4. Notice that, even though the actuators have different spring constants and motor inertias, the natural frequencies are all between 10 and 20 rad/sec.

**Table 3.5** uBot-7 SEA joint natural frequencies

	Spring Constant (Nm/deg)	Motor Inertia (gcm <sup>2</sup> )	Reduction (N:1)	Natural Frequency (rad/sec)
Torso	3	181	159	19.39
Shoulder Flexion	11.25	3060	113	12.85
Shoulder Abduction	5.25	181	260	15.68
Shoulder Twist	3	181	159	19.39
Elbow	3	181	159	19.39

To simplify fabrication, the springs were designed such that they can be installed with screws only. The design was created such that they would not slip under operational loading due to the frictional interface caused by the screw tension. To maintain proper frictional interface, the screws must be torqued to the specifications shown in Table 3.6 [47].

**Table 3.6** Tightening torque for spring screws [47]

Screw Type	Tightening Torque (Nm)
M3 Flat Head Cap Screw	2.48
M3 Socket Head Cap Screw	5.85
M4 Flat Head Cap Screw	1.85
M4 Socket Head Cap Screw	3.4

### 3.6 Arm Design

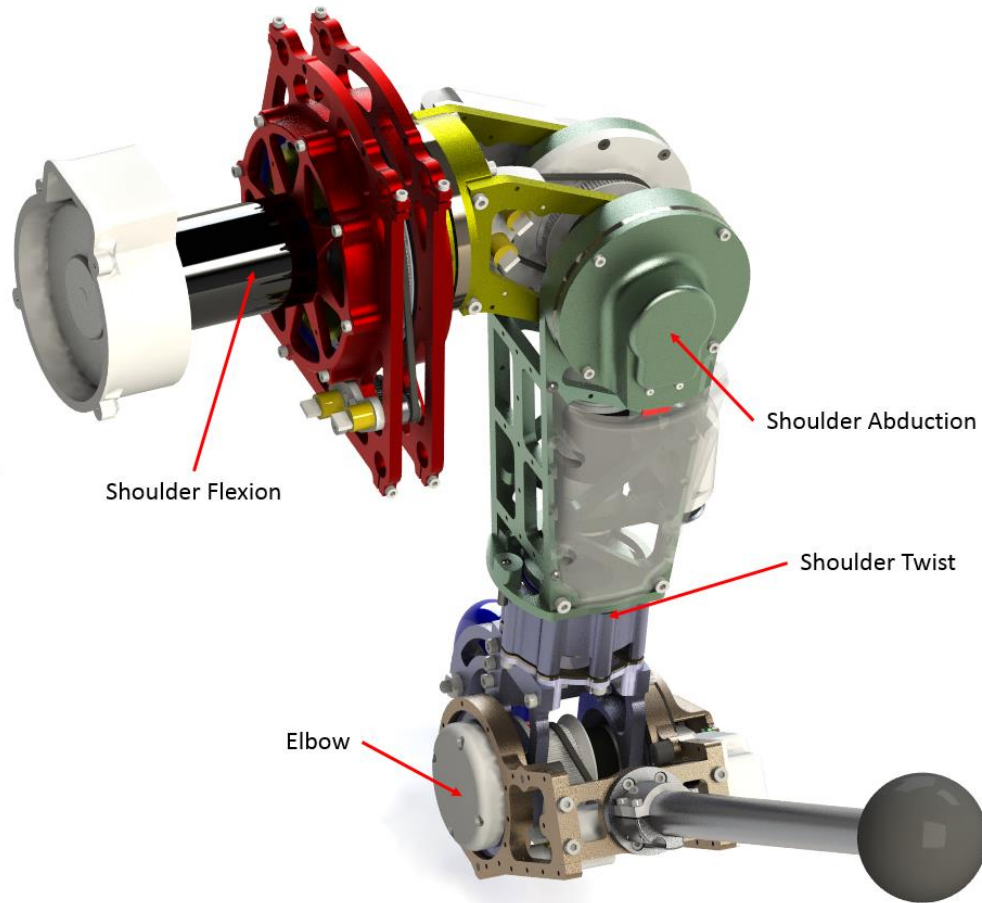


**Figure 3.11** Rendering of uBot-7 arm CAD model

This section discusses the uBot-7 arm which is shown above in Figure 3.11. To reduce mechanical components used, the arm consists of a serial kinematic chain. The color coding of this model is such that the parts that are the same color do not move relative to each other. Notice that there are 5 colors and therefore 4 joints in the arm. These joints are referred to as the shoulder flexion joint (red/yellow), shoulder abduction joint (yellow/green), shoulder twist joint (green/purple), and the elbow joint (purple/bronze). All of these joints consist of a brushless DC motor, spring, link that is constrained by two ball bearings, an absolute position sensor, and a deflection sensor. A local control unit will also be added to the joint once the electrical design is finished, but that is beyond the scope of this thesis.

### 3.6.1 Shoulder Flexion

The shoulder flexion joint of uBot-6 can be seen below. It consists of a 48 watt brushed DC motor with a planetary gearhead (159:1). This gearhead is connected to the cable mechanism shown in Figure 3.12 which has a 2:1 reduction. One advantage of this mechanism is that there is plenty of space for cable routing as the axis of rotation of this joint is hollow. The joint uses an absolute position sensor to measure position when starting. This sensor is connected to the joint through a belt mechanism with a reduction and therefore the joint must be started in the correct range of positions.

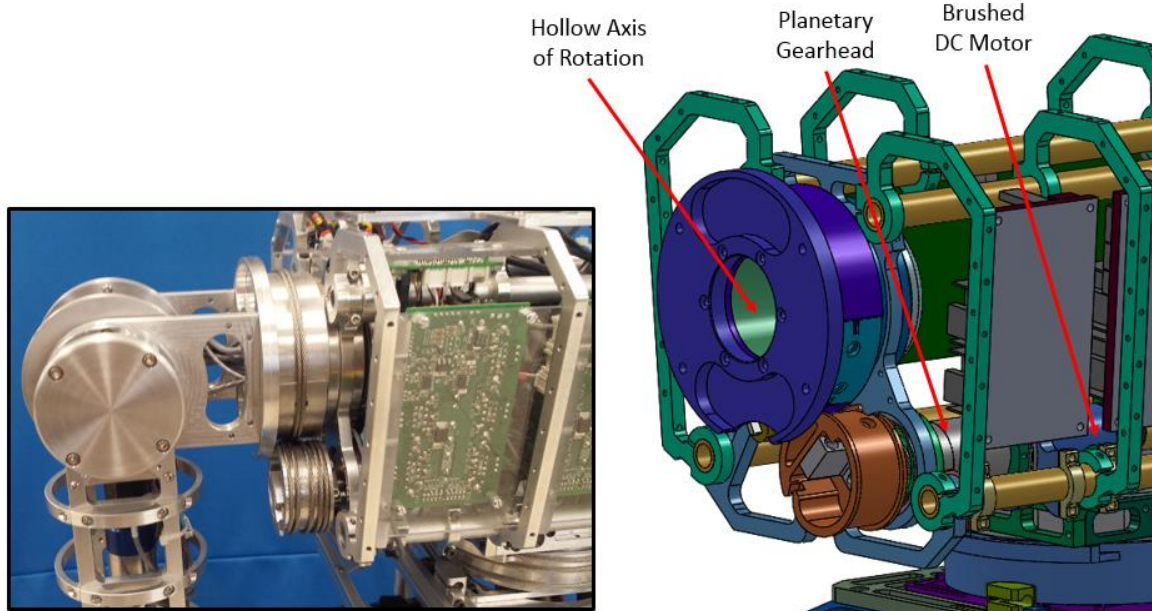


**Figure 3.12** uBot-6 shoulder flexion joint

The uBot-7 shoulder flexion joint can be seen in Figure 3.13. This joint differs from the uBot-6 equivalent in ways other than the addition of compliance. The cable mechanism in uBot-6 introduced more components to the system and a significant radial load on the gearhead with the benefit of an empty axis of rotation. Because of the new embedded system, fewer wires pass through the joint and therefore less space for wires is required. For this reason, the cable

mechanism was replaced by a joint driven directly by a planetary gearhead. The wires still pass through the bearings in this joint but are wrapped around the shaft extender.

A keyless tapered bushing was used to connect the motor shaft to the shaft extender as it can handle high torques (81 Nm) [48]. The motor used was an EC 90 Flat brushless DC motor with a GP 52 C gearhead that has a 113:1 reduction. This is actually the smallest reduction of all the joints even though it has the highest torque. This is made possible by the high torque constant of the motor. A motor cover is necessary because the motor windings are not sealed from the environment.

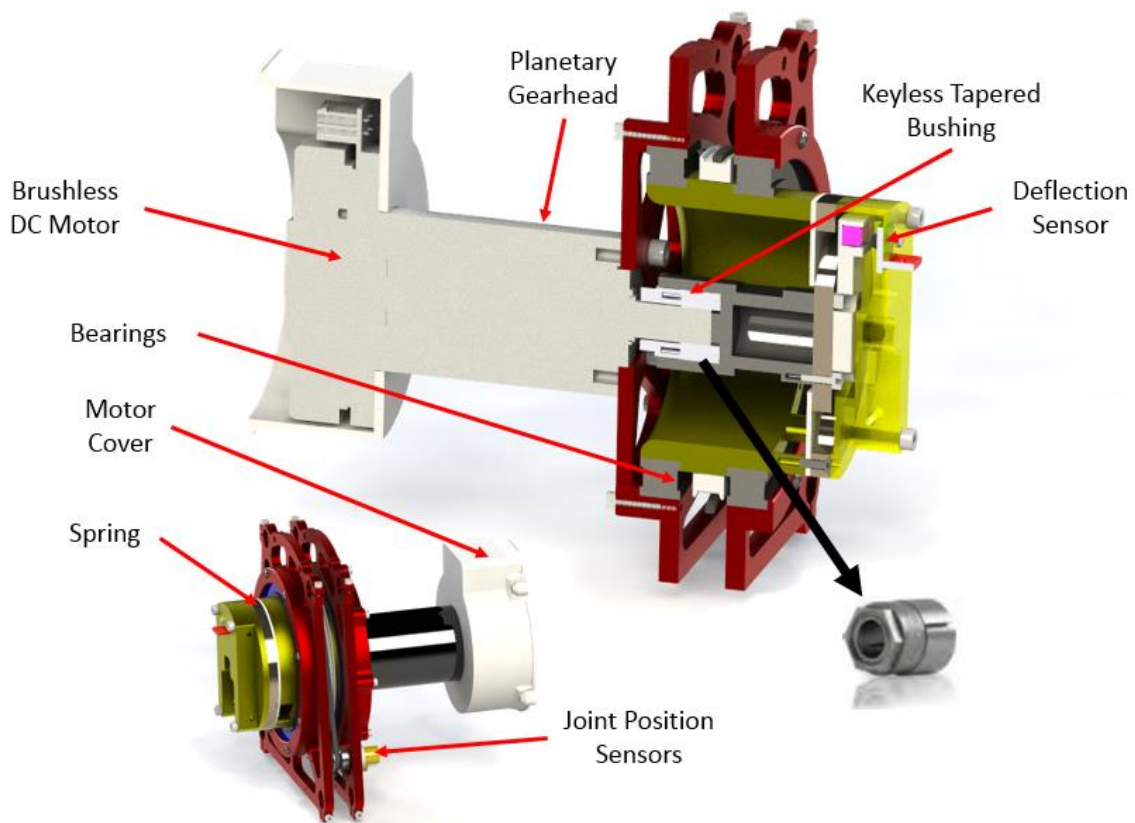


**Figure 3.13** uBot-7 shoulder flexion joint, cross-sectional view of joint, and keyless tapered bushing used [48]



### 3.6.2 Shoulder Abduction

The uBot-6 shoulder abduction can be seen in Figure 3.14. This joint is similar to the uBot-7 shoulder flexion joint in the sense that it is directly driven from the gearhead output shaft. The motor sits inside of the bearings that support the joint to save space. As with the uBot-6 shoulder flexion, the absolute position sensor on the joint is driven by a belt mechanism with a reduction. Because of this the robot must be started up within a certain range.

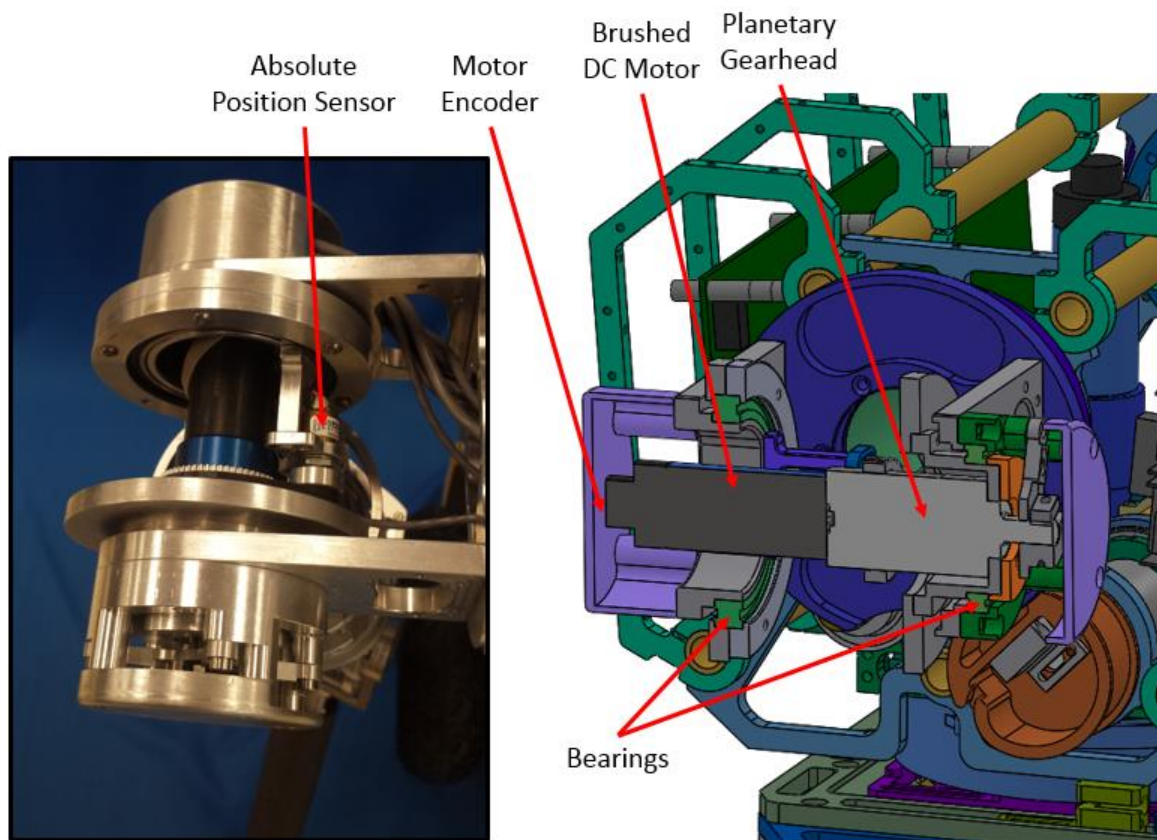


**Figure 3.14** uBot-6 shoulder abduction joint

The uBot-7 shoulder abduction mechanism is similar to its predecessor and can be seen in Figure 3.15. In this joint, the motor and gearhead also sit inside of the joint bearings to save space. The spring in this joint (as well as all of other uBot-7 SEA joints) acts as a flexible shaft coupling and reduces radial loading on the gearhead shaft due to misalignment. The uBot-6



shoulder flexion and shoulder abduction axes of rotation intersect. This is not the case in the uBot-7 which has shoulders that slightly “droop”. This is due to the angle of the input link, shown in yellow, and increases the range of motion of the arms. This moves the joint axis of rotation forward relative to the chest when reaching forward and thus reduces the arms interference with the chest.

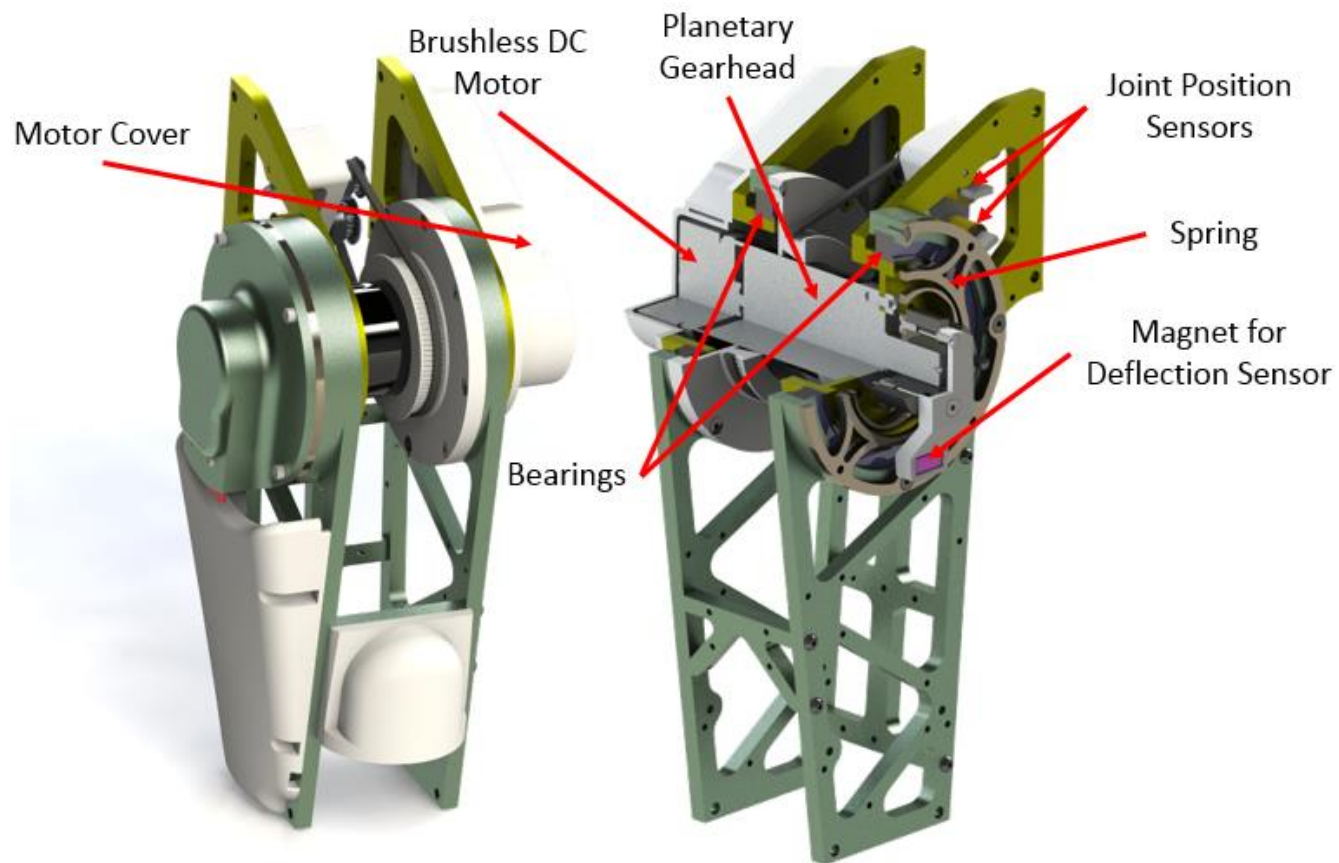


**Figure 3.15** uBot-7 shoulder abduction joint

### 3.6.3 Shoulder Twist

The uBot-6 shoulder twist joint functionally resembles the uBot-7 shoulder flexion joint. This joint can be seen in Figure 3.16 and Figure 3.17 and has a shaft that is rigidly connected to the motor shaft. This extends through a bore and is connected to the output of the joint on the far side of this bore. Because the shaft is significantly smaller than the bore, wires can be passed through this space. The absolute position sensor is driven by a belt in which the driver pulley is on the extended shaft. One reoccurring problem with this joint, as well as some of the other uBot-6 joints, was the attachment method between the gearhead shaft and the shaft extender. This connection can be seen in Figure 3.16. The motor shaft has a flat on it and the shaft extender is clamped to this piece as shown. In this configuration, the screws would stretch and break when the joint is heavily loaded.

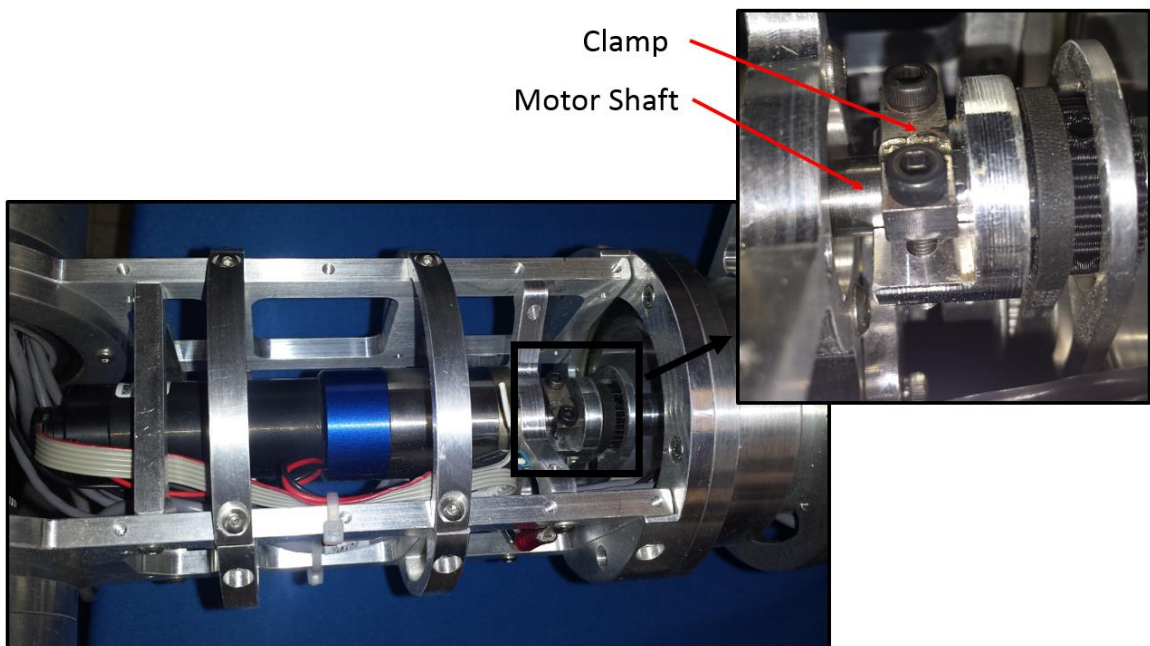


**Figure 3.16** uBot-6 shoulder twist shaft connector clamp

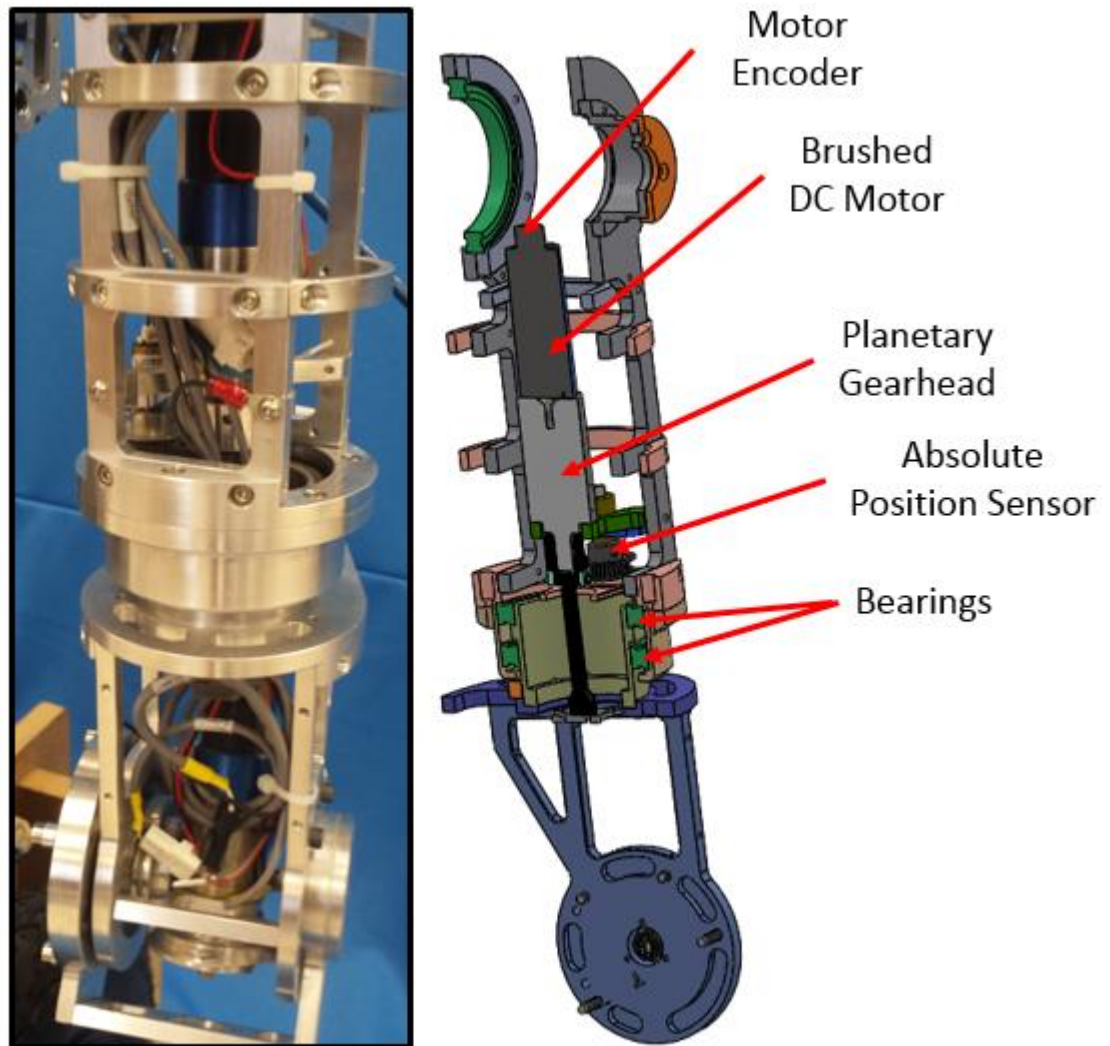


**Figure 3.17** uBot-6 shoulder twist joint

The uBot-7 shoulder twist is similar to the uBot-6 joint and can be seen Figure 3.17. One major change is the shaft extender connection. Instead of the clamp shown in Figure 3.16, a tapered bushing was used. This bushing is capable of 18 Nm of torque before slipping occurs according to the manufacturer's datasheet [49]. When using these tapered bushings, removal becomes difficult without a means of pushing/pulling the mating components apart. This is why the threaded hole was added at the end of the shaft extender. The M8 threads allow the components to be easily pushed apart when desired. Another change was to make the absolute

position sensor ratio to 1:1. Since this joint can only rotate a little bit less than  $360^\circ$ , this ratio results in a unique position throughout the whole range of motion.

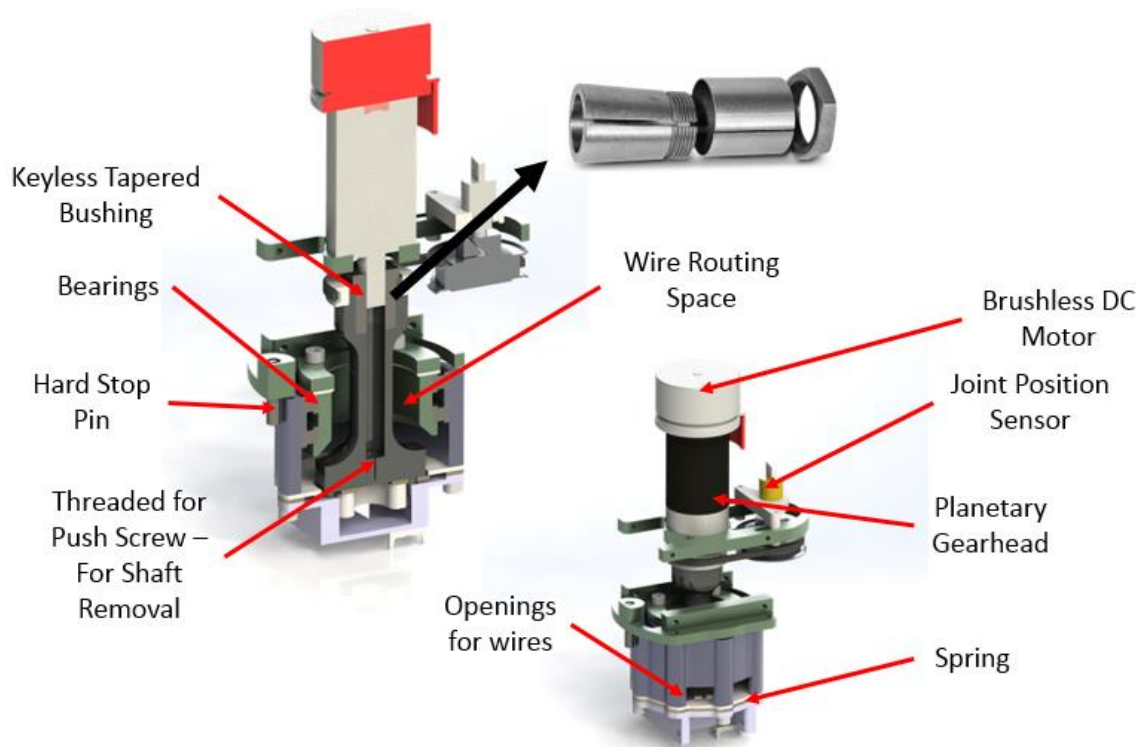


**Figure 3.18** uBot 7 shoulder twist joint and the tapered bushing used [49]



### 3.6.4 Elbow

The elbow joint in uBot-6, shown in Figure 3.19, used a right angle cable drive mechanism to attain a desirable form factor. Since the motor gearhead combinations used were 108 mm long, a joint identical to the uBot-6 shoulder abduction would be too wide and would interfere with torso, reducing the arm's range of motion. Another important feature of this joint is the wheel added to the backside of the elbow. This enables the prone scooting mobility modes shown in Figure 2.5.

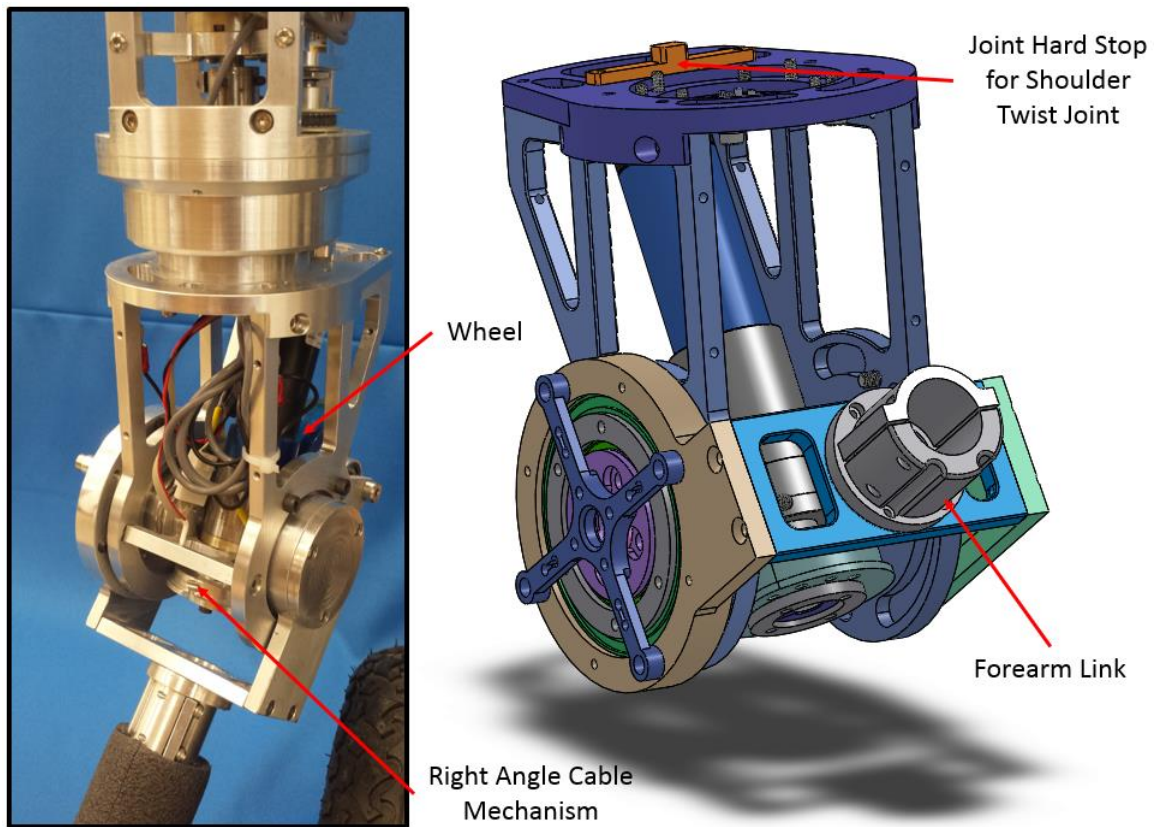


**Figure 3.19** uBot-6 elbow joint

The uBot-7 elbow joint is shown in Figure 3.20 and was designed to reduce mechanical components by eliminating the cable mechanism. This was made possible through the use of a shorter motor gearhead combination. The mechanism is functionally similar to the shoulder

abduction mechanism shown in Figure 3.15 where the gearhead output shaft is rigidly connected to the spring. As previously stated, the spring acts as a flexible shaft coupling in addition to its primary purpose as a compliant element in the SEA. This joint has a 3:1 reduction on the position sensor, but since the joint only rotates  $120^\circ$ , this reduction still results in a unique position signal throughout the whole range of motion. Another important thing to note is that this joint, as well as the other uBot-7 arm joints, have a hard stop limiting the spring deflection to  $\pm 4^\circ$ .

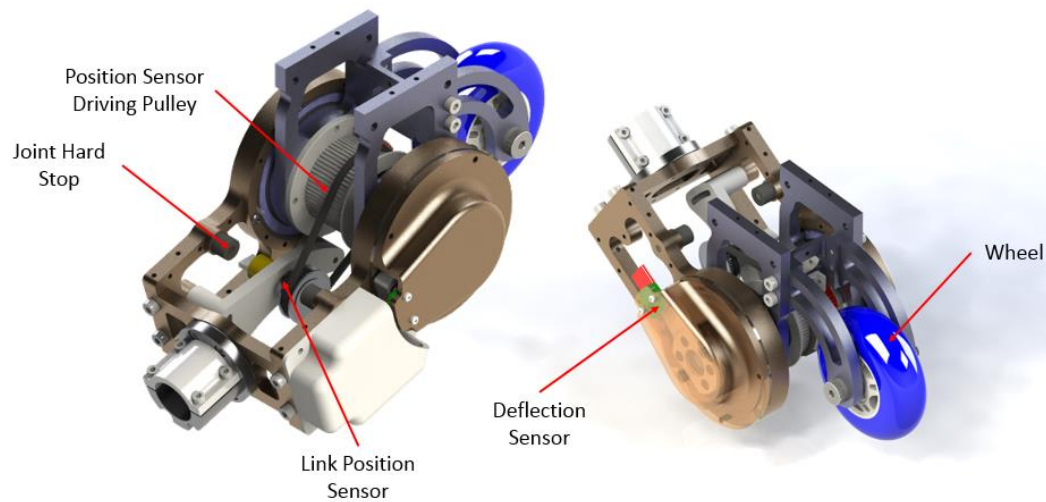


**Figure 3.20** uBot-7 elbow joint

### 3.7 Torso Design

The uBot-6 torso design is shown in Figure 3.21 and is very similar to the uBot-6 shoulder flexion joint design. Due to the location of electronics, many wires must pass through this joint (as discussed in Section 3.9, *Distributed Embedded System*) and therefore this design was chosen to increase the space in the center of the joint. One important thing to note about this is that when wires pass through the center of a joint, effects of twisting the wires are minimized.

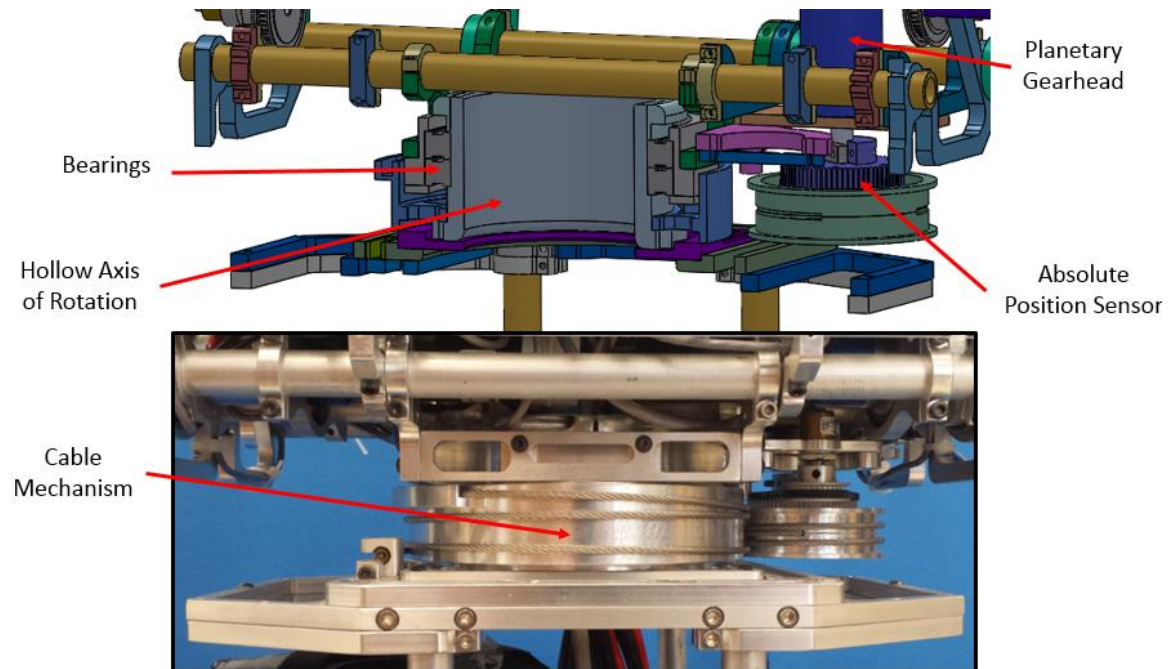


**Figure 3.21** uBot-6 torso joint

The uBot-7 torso design is shown Figure 3.22. As in the shoulder flexion joint, this joint also deviated from the cable drive mechanism to reduce the number of mechanical components and the radial loading on the gearhead shaft. The chest was also rounded and narrowed at the sides closest to the arms to increase the range of motion of the robot as can be seen in the bottom of Figure 3.22. The chest is also capable of folding open with the removal of two thumb screws to allow access to the components inside.

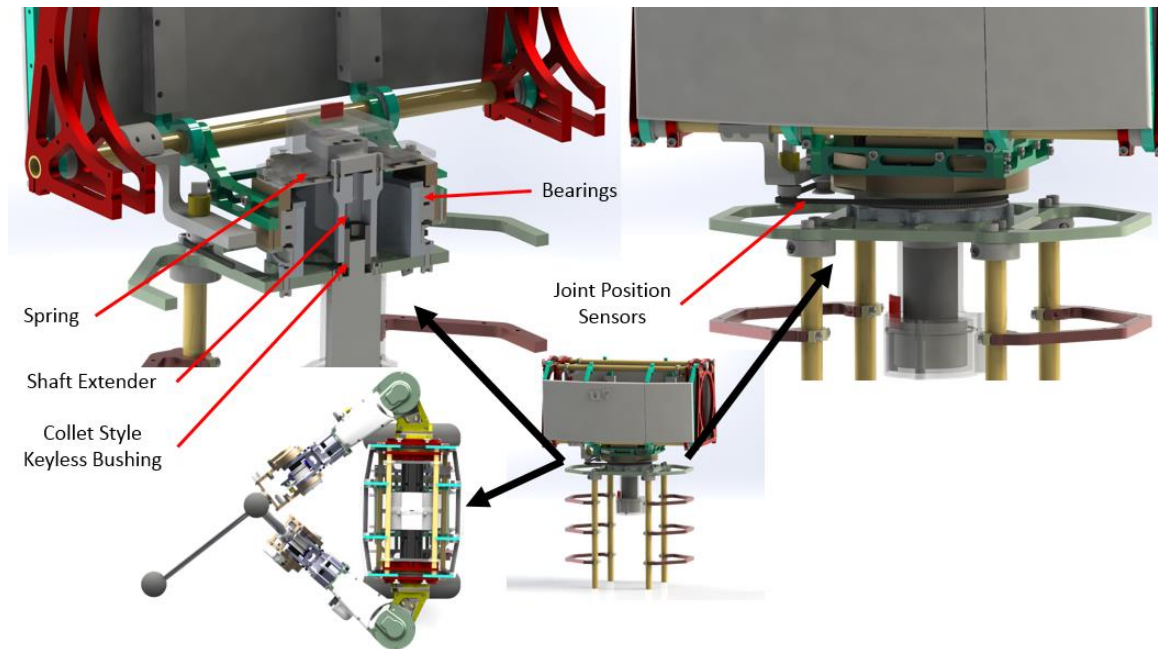


**Figure 3.22** uBot-7 torso joint



### 3.8 Drivetrain Design

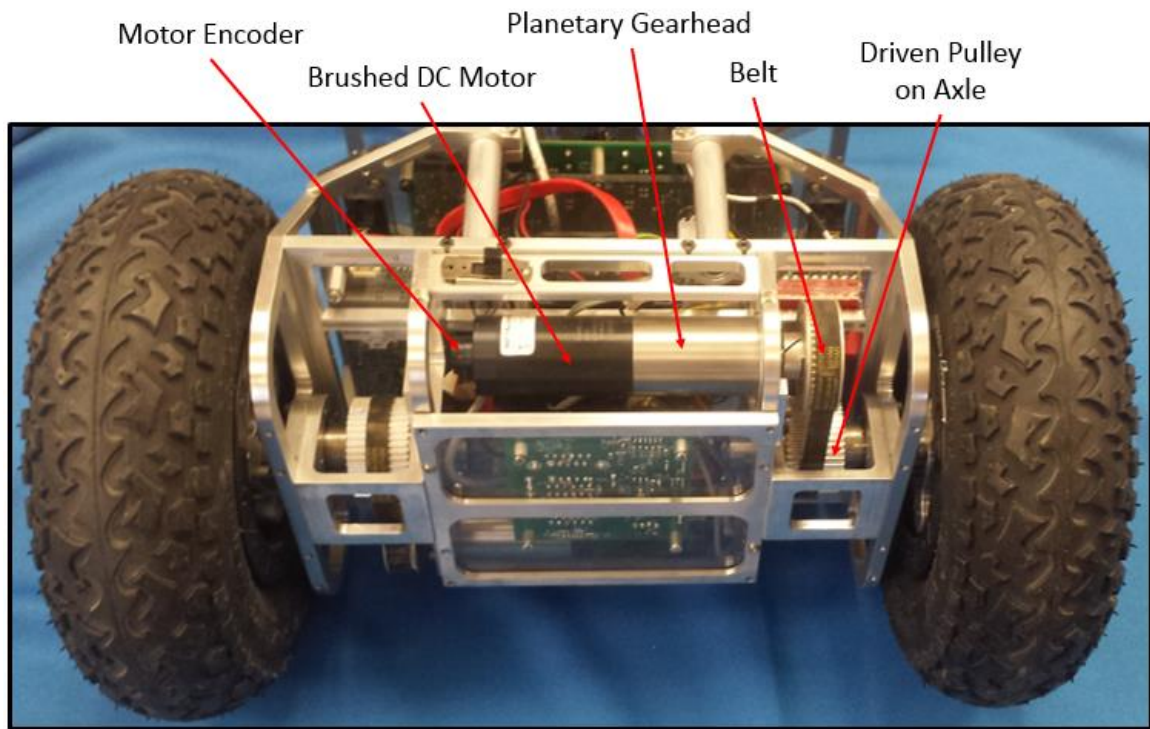


**Figure 3.23** uBot-6 drivetrain mechanism

The uBot-6 drivetrain uses a DC motor with a planetary gearhead connected to each wheel through a belt mechanism that has a 1:1 ratio as shown above. This mechanism is capable of a maximum torque of 5.7 Nm, a continuous torque of 3.3 Nm and a no load speed of 138 rpm. The drivetrain has been proven to work, however, the planetary gearhead introduces  $\sim 1^\circ$  of backlash into the system. This results in a nonlinear effect of a dead band when the direction of motor torque changes. In some applications this does not greatly affect performance, however, since the uBot is normally balancing in a vertical position the motor torque is almost always fluctuating around zero causing effects of backlash to become apparent. This results in the uBot constantly oscillating back and forth a small amount.

To minimize the balancer oscillations and to make it possible to implement a more robust controller the uBot-7 uses a new drivetrain mechanism that consists of a belt driven directly by the motor shaft as seen in Figure 3.24. When properly tensioned, this design has near zero backlash. The pulleys create a reduction of 7.5:1. With the high torque motor used, the maximum intermittent torque is 7.5 Nm and, the maximum continuous torque of the mechanism is 2.5 Nm. The no load speed of the mechanism is 282 rpm. Both the driver pulley shaft and the wheel shaft are supported by two ball bearings that are pressed into the green and blue blocks shown in the below figure respectively.

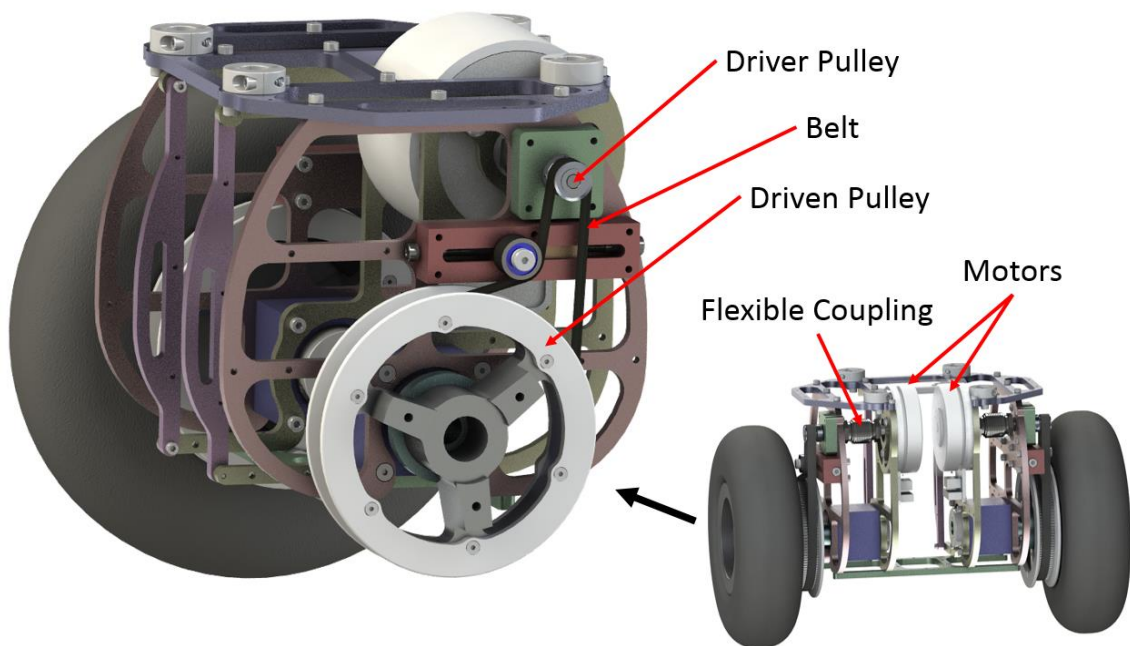


**Figure 3.24** uBot-7 drivetrain Mechanism

### 3.9 Distributed Embedded System

Since the uBot-6 embedded control system was designed, technology has advanced such that commercially available motor controllers are available that are small enough to place at joints while still maintaining power ratings high enough to drive the motors at their maximum power rating. This makes it possible to implement a distributed embedded system on the robot that has advantages over uBot-6's embedded system outlined in Figure 3.25. Note that in this system the FPGA runs the control loops and the H-Bridges amplify the power signal from the FPGA to supply motor with adequate power. In this section the outline of the new and old embedded system is discussed as this had effects on the mechanical system. The full development and implementation of the system is beyond the work of this thesis.

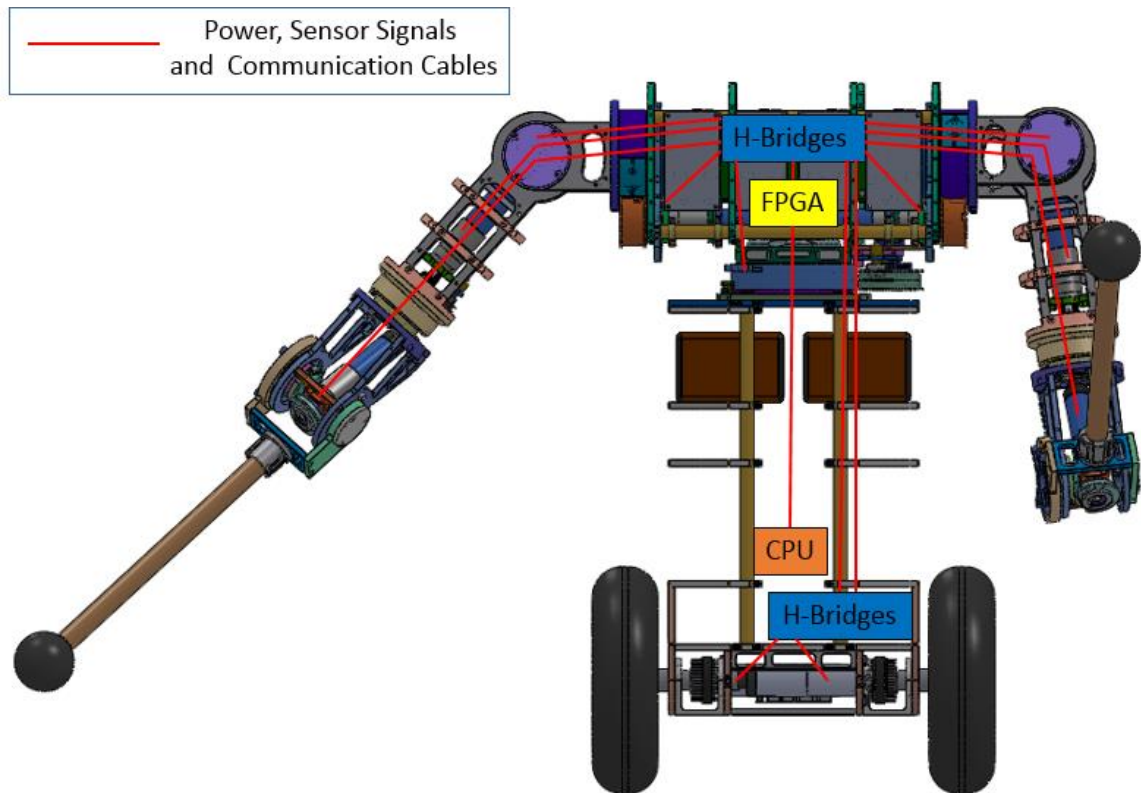


**Figure 3.25** Layout of uBot-6's embedded system

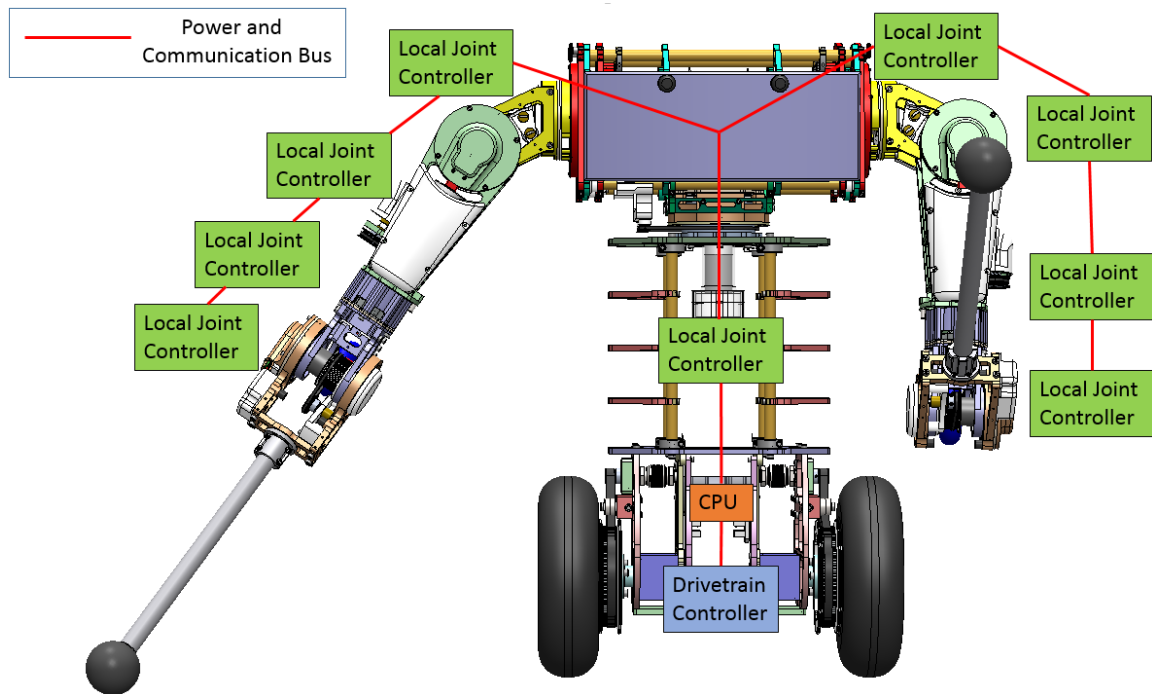


**Figure 3.26** Outline of the uBot-7 distributed embedded system

A distributed embedded system, as shown in Figure 3.26, has advantages over a centralized embedded system like the one implemented in uBot-6. First of all, in a centralized embedded system, all of the wires in the arms must travel to the chest, where the signals are processed, thus resulting in a large number of wires crossing joints. Since SEAs have more sensors than position controlled actuators, an increased number of wires must travel to a signal processor, and this problem is increased. When using local controllers, these signals are processed at the joint and therefore the wires only need to cross a maximum of one joint thus greatly reducing the numbers of wire crossings. This also reduces the distance signals have to travel thus reducing the noise in these signals. Since the arms are 4-DOF, the number of wires are decreased by a factor of 3 at the shoulder flexion joint. Each local joint controller has connectors allowing easy removal of electrical connections which enables assembly/disassembly for maintenance and repairs to be completed with less wire burden. As stated in [15], wires

crossing joints is also a common point of failure. This means that reducing the wires can increase the reliability of the robot. The new embedded system also creates more free space in the body of the robot. This is beneficial as extra space can be used for extra batteries, CPUs, or any other number of things that may be later implemented on the platform. The new system also allows for the addition of new components such as a neck, end effector, or GPU with minimal restructuring of hardware.

### 3.10 uBot-7 Mechanical Design Summary



**Figure 3.27** Base and torso of uBot-7

The new uBot SEAs were implemented in two, 4 DOF arms and a 1 DOF torso. Higher power motors were chosen for the robot to increase controllability while also allowing tasks requiring higher torques to be completed. The gearheads were chosen such that the torque and speed target specifications were met while maintaining loads within the gearhead manufactures ratings. The springs were chosen in such a way that spring deflection would occur over a small range and that the max deflection torque corresponds to the max actuator torque. This allows the torque to be measured over the full range of statically controllable torques. Lastly, a new embedded system is implemented and the wheel mechanism has been improved to have reduced backlash. A summary of the uBot-7's size and weight can be seen in Table 3.7 and can be compared to that of uBot-5 and uBot-6.

**Table 3.7** uBot-6 and uBot-7 size and weight  
(\*based on CAD model not actual weight)

		uBot-5	uBot-6	uBot-7
Body	Height (mm)	605	710	740
	Shoulder Width (mm)	575	603	650
	Base Width (mm)	400	405	410
	Weight (kg)	19.5	24.3	26*
Arms	Shoulder Link Length (mm)	110	112	113
	Upper Arm Link Length (mm)	254	330	300
	Forearm Link Length (mm)	236	365	400

Figure 3.29 shows the sections of the uBot-7 arm that move relative to the torso. The total mass of these parts as taken from the CAD model is 4.97 kg compared to the 3.94 kg of uBot-6 arm. The center of mass of this system is 240 mm from the body of the robot when the arm is fully elongated. This can be compared to the uBot-6 arm shown in Figure 3.28 where the center of mass occurs at 274 mm from the body.

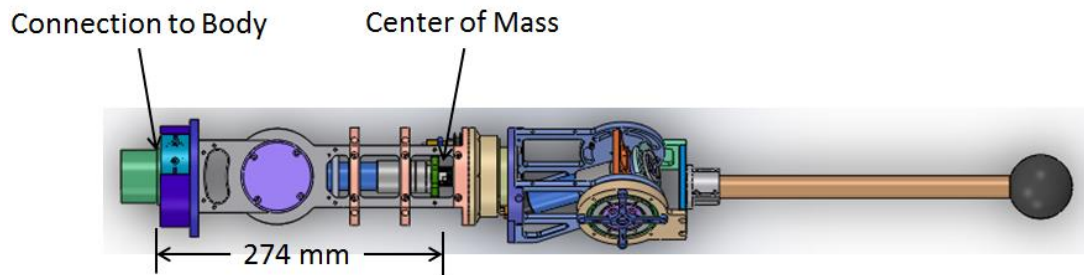


**Figure 3.28** uBot-6 arm center of mass location

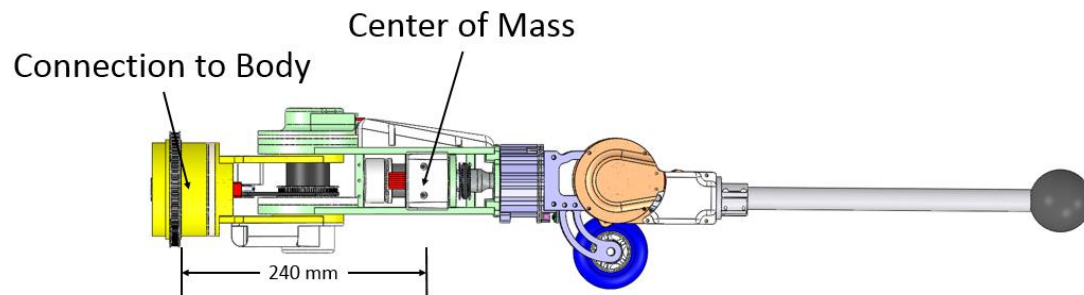


**Figure 3.29** uBot-7 arm center of mass location

In conclusion, the uBot-7 is about 4 cm taller and wider than uBot-6 and will likely weigh slightly more. The major contributors to the increased weight of the platform include: larger motors at proximal arm joints, more robust gearheads to meet rated loads, and added components required for SEAs. Even though the arms are heavier, the center of mass location is closer to the body of the robot which lowers the arm inertia.



## CHAPTER 4

### SENSOR DESIGN

Typically, SEAs use at least two feedback measurements to calculate joint position and joint torque. Most SEAs use position sensors while some use a load cell to more accurately measure torque [21]–[24], however, commercially available load cells are expensive and custom load cells require significant development effort. Most SEAs measure spring deflection to get torque feedback [15], [20], [25]–[27], [29]. It is important to note that spring deflection can be directly measured or can be calculated from the equation below where joint output position ( $\theta_L$ ), and motor position ( $\theta_m$ ), are measured to calculate spring deflection ( $\theta_s$ )

$$\theta_s = \theta_L - \theta_m \quad (4.1)$$

Due to the backlash in the planetary gearheads and given the small deflection range in the uBot-7, it is necessary to measure spring deflection directly in order to obtain an accurate joint torque. It is also advantageous to measure joint output position directly instead of motor position measurement after the backlash. This results in positioning errors that compound through a kinematic chain. It is desirable to measure position with absolute versus incremental sensors to avoid a calibration routine at every system start-up which can be time consuming due to the number of joints. It can also be difficult to do accurately as the joints must be placed in known position and force configurations.

The uBot-7 sensor configuration includes an absolute measurement of joint link position and an absolute measurement of spring deflection that is measured directly across the spring. The motor position is also measured using the Hall effect sensors on the motor. This gives a low resolution signal that was not used in this thesis but may be used in the future.

#### 4.1 Spring Deflection Sensor

In order to implement an accurate torque controller it is necessary to have a high resolution spring deflection sensor. From equation (4.1) it can be seen that the difference between motor position and joint output position can be measured to get spring deflection as done in [15]. This method works when there is minimal backlash in gear train between the sensors, but is subject to compounding noise from two sensors. Another method involves measuring motor position and spring deflection (the difference in output link position and motor position) directly as done in [20] which allows for more accurate spring deflection measurement, however, does not directly measure output position and therefore may have effects from compounding position errors when implemented in a kinematic chain. The third method of measurement in a SEA is by measuring spring deflection and output position as done in [24, 26]. This minimizes positioning errors while maintaining accurate spring deflection measurement. As previously mentioned, some SEAs use a load cell in addition to measuring spring deflection.

In the case of uBot-7, the gearheads have  $\sim 1^\circ$  of backlash and a load cell would be too expensive and add bulk. Therefore, spring deflection is measured directly and has a range of  $\pm 4^\circ$ . Using traditional rotary position sensors would only utilize  $8^\circ/360^\circ$ , or 2.2%, of their range and thus reduces resolution. To address this problem a custom deflection sensor was designed to measure only the deflection range with high resolution using a 14-bit Hall effect sensor.

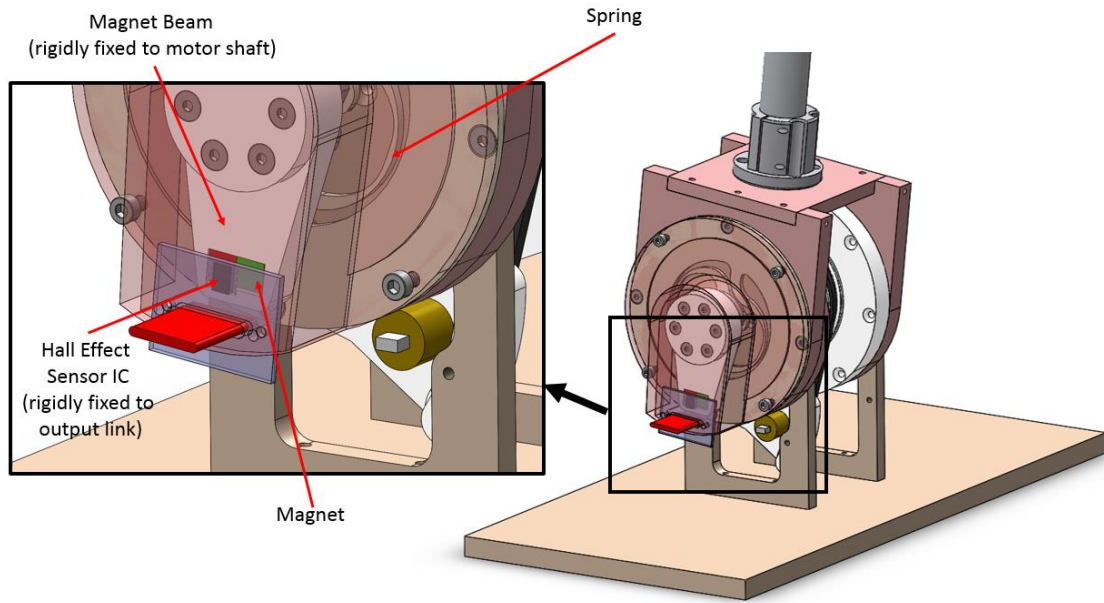


**Figure 4.1** Deflection sensor configuration

As seen in Figure 4.1, the deflection sensor consists of a magnet that is held at a radius on a beam that is rigidly connected to the motor shaft. A Hall effect sensor is fixed above the magnet and rigidly connected to the output of the joint. Since the rotation of the motor shaft relative to the output of the joint is only  $\pm 4^\circ$ , the assumption can be made that the trajectory of the magnet with respect to the sensor is linear. The red arrows in Figure 4.2 indicates the trajectory of the sensor relative to a rectangular neodymium magnet. The colors in the plot represent the magnitude of the magnetic flux density ( $|B|$ ). The sensor only measures the Z component of this magnitude which is normal to the surface of the sensor. Figure 4.3, in blue, shows the simulated magnetic flux density in the Z direction vs. position of the sensor in the Y direction. Zero position corresponds to the center of the magnet. It can be seen that there is a linear relationship between these two variables that has an  $R^2$  value of 0.9995 over a linear displacement of  $\pm 4\text{mm}$ . The simulation was done such that only movement in the Y direction occurred and no movement in the Z direction was present. This linear range is specific to the simulated magnet and the size varies depending on air gap and magnet used. It is important to

note that this configuration can be modified to work in different scenarios by adjusting the air gap size, changing the beam length, or by using different magnets.

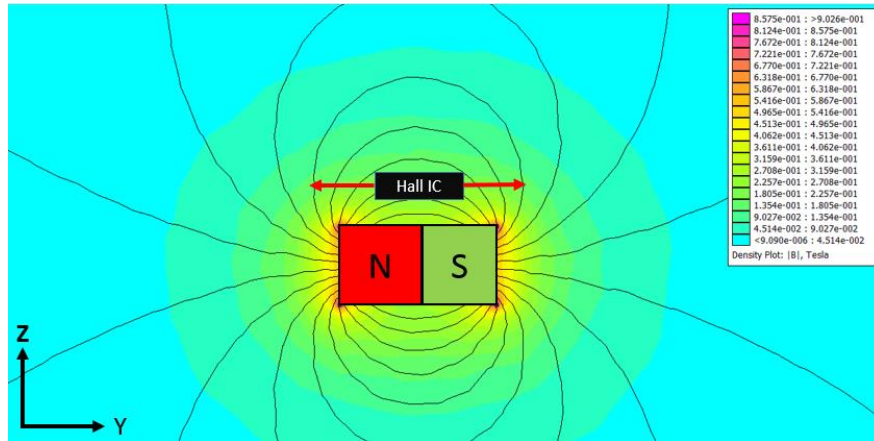


**Figure 4.2** Sensor movement (indicated by red arrows) within the magnet field of a rectangular neodymium magnet. The colors correspond to the magnitude of the magnetic flux density ( $|B|$ ) of the field. Simulation done using FEMM software[50]

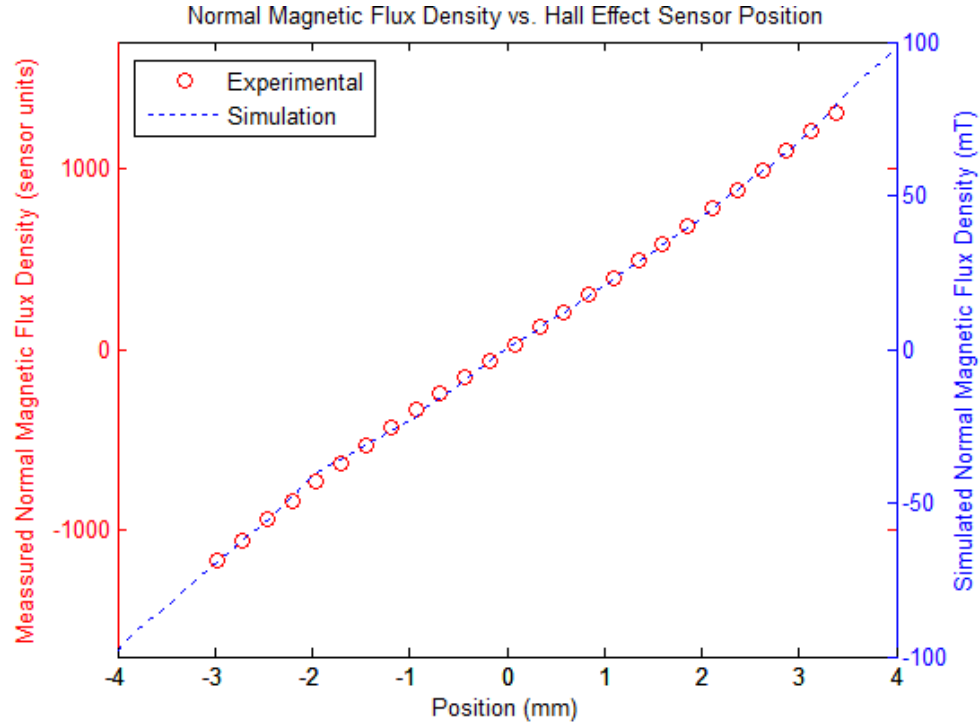


**Figure 4.3** Normal magnetic flux density vs. position from simulation and experimentation on micrometer stage

## 4.2 Deflection Sensor Design Steps

To design the highest resolution deflection sensor the following design steps were followed:

Step 1: Select the maximum deflection angle,  $\vartheta$ , to be measured,  $\pm 4^\circ$  in this case. Note that this sensor will only be accurate for small angles and will likely not work once the small angle approximation is no longer valid.

Step 2: Determine the magnet beam length,  $r$ . For maximum resolution, the beam length should be maximized to increase linear displacement. However, this is likely constrained by the available space within the assembly. The magnets linear displacement,  $d$ , can be determined by:  $d = 2 * r \sin \theta$  in this case  $\vartheta = 4^\circ$ ,  $r = 35\text{mm}$ , and  $d = 5\text{mm}$ .

Step 3: Determine magnet. The linear region of the magnetic flux density is less than the width of the magnet and thus the magnet must be wider than the displacement,  $d$ , calculated in Step 2. The magnetization of the magnet needs to be oriented parallel to the path of motion of the sensor similar to the magnet shown in Figure 4.2. The magnet should be capable of reaching the maximum measurable magnetic flux density of the sensor at max displacement. It is also important to note that magnet must have sufficient depth (in the X-direction of Figure 4.2) such that slight changes in this direction do not affect the signal.

Step 4: Determine air gap distance. The air gap is defined as the distance between the surface of the magnet and the sensor. At the maximum displacement ( $d/2$ ), plot the magnetic flux density in the Z direction as a function of air gap size. Note the maximum magnetic flux density that the sensor can measure. This results in a graph similar to the one shown in Figure 4.4, where the blue line indicates the normal magnetic flux density and the red line indicates the maximum measurable value. Notice that at very low air gaps there is a positive slope. To reach the range in which deflection is linearly proportional to normal magnetic flux density the air gap

must be larger than the value where this peak occurs. The lines intersect at 2.5 mm, and thus this was the air gap chosen for the example setup. Note that this air gap corresponds to the distance between the Hall effect sensor and the magnet, not the top of the integrated circuit package that houses the sensor.

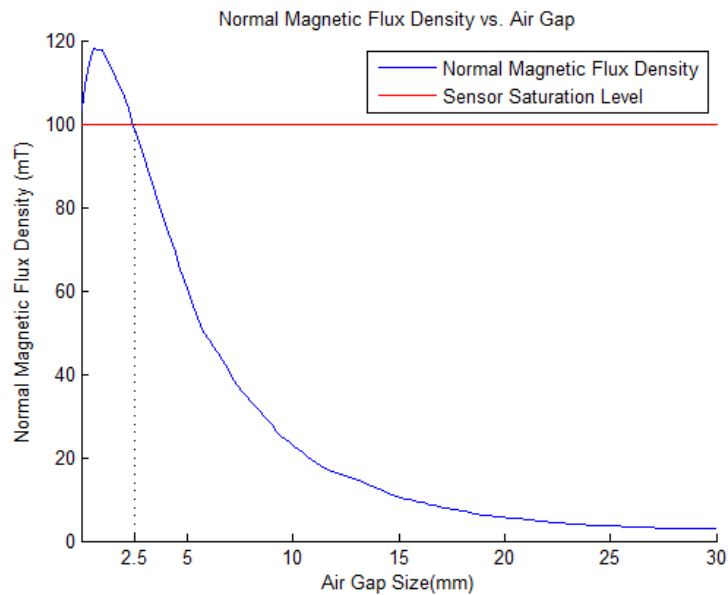


**Figure 4.4** Magnetic Flux Density in the Z direction (normal to surface of ic) at maximum displacement (4mm) vs. air gap size

### 4.3 Experimental Validation

To validate the simulation, a B448 magnet from K&J Magnetics and a Melexis 90363 Hall effect sensor were used. The magnet was suspended 2.5mm over the sensor which was fixed to a micrometer positioning stage as seen in Figure 4.5. For the first test, the sensor was moved 6mm across the sensor and 26 data points were taken. The data was then offset so the zero crossing occurred at the origin. The simulated and experimental results are shown in Figure 4.3. The data was linear with an  $R^2$  value of 0.9993.

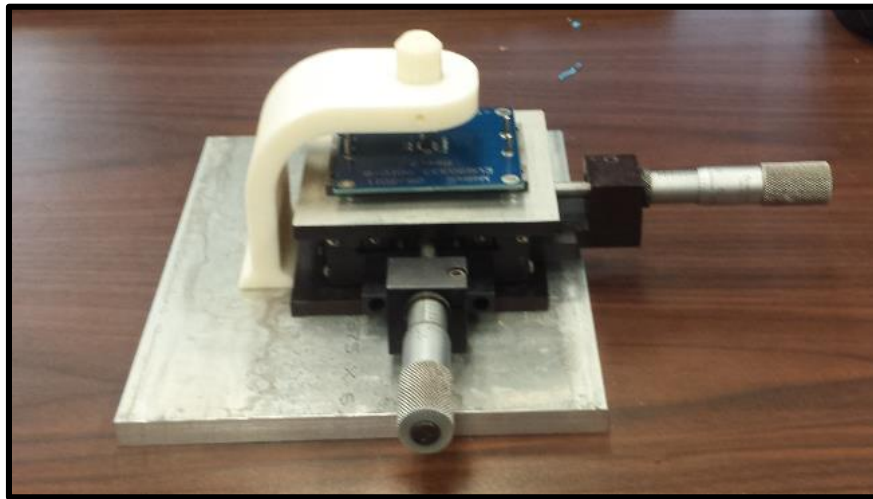


**Figure 4.5** Micrometer stage setup used to test sensor

Noise was evaluated from the sensor in three static positions and it was found that there was a standard deviation of 5.1 sensor units (for 3000 data points). For this setup, only 12-bits from the sensor are usable and thus the noise corresponds to  $0.01^\circ$ . Once the sensor was installed on the SEA prototype, it was also found that the sensor had repeatable offset corresponding to the output position of the joint likely due to small movements in the mechanical system causing small changes in the magnets position relative to the sensor. This offset is repeatable and therefore can be calibrated in order to retain performance.

#### 4.4 Absolute Position Sensor

If the system has backlash, then it is important to measure the output link position, as opposed to motor position, in order to accurately control the end point position. The backlash from one joint may result in a small error at that joint but this has compounding effects throughout a kinematic chain. It is also desirable that this position be taken as an absolute measurement versus an incremental measurement so that there is no calibration routine required when starting the robot. To accomplish this an absolute position sensor was connected to the joint with a belt and pulley. Due to size limitations a unique configuration was used. A belt mechanism located the sensor suitably and a reduction was used to decrease the size of the sensor pulley. Because of this reduction, the signal from the sensor did not correspond to a unique joint position. To address this issue, two sensors were used and driven by a belt. The sensor pulleys were sized slightly differently causing a shift in signals corresponding to joint position. Because of this, the combination of sensor signals results in a unique signature for each position that the joint travels. Figure 4.6 shows an example of the pulleys used in the shoulder flexion joint.

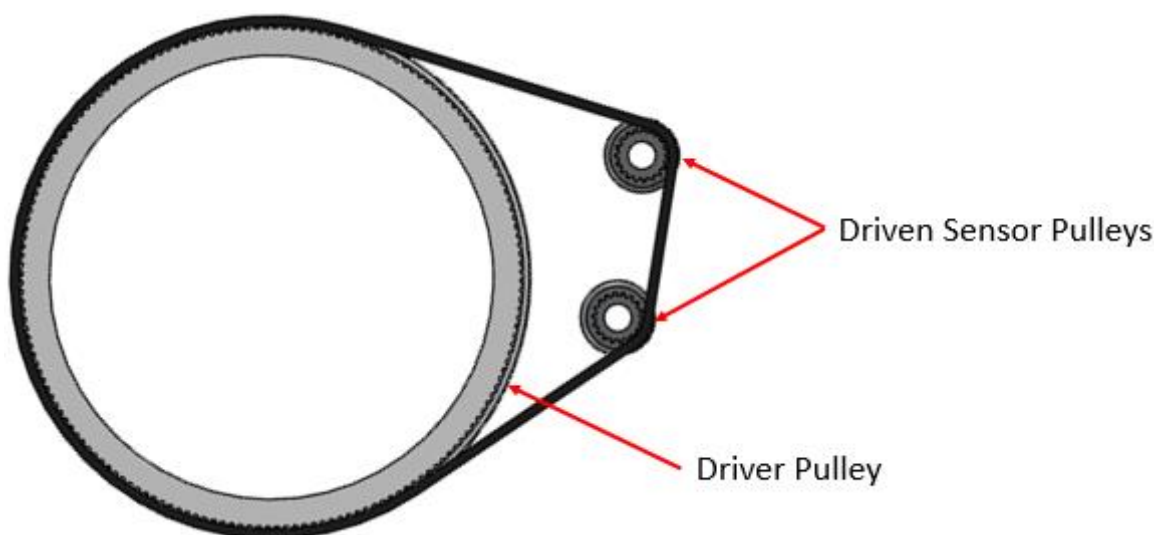


**Figure 4.6** Absolution position sensor pulley configuration for uBot-7 shoulder flexion joint



As an example, the shoulder flexion joint has a  $720^\circ$  range of motion. Within this range of motion each position must be uniquely identified. To do this, a driver pulley with 172 teeth is used to drive two pulleys, one with 18 teeth and the other with 19 teeth. These two driven pulleys are connected to rotational absolute position sensors. The sensors used for this implementation were MA3 Miniature Absolute Magnetic Shaft Encoders from US Digital that output a 10-bit PWM signal at 1000 Hz. By measuring the difference in position between the two driver pulleys, the position can be uniquely identified. This is depicted in Figure 4.7 where the red and green lines indicate the individual position sensors and the blue indicates the unique signal that can be calculated from these sensors. This signal would be multiplied by 2 to get the joint position. Note that this is similar to finding the phase shift between two curves with different frequencies when operating in the time domain.

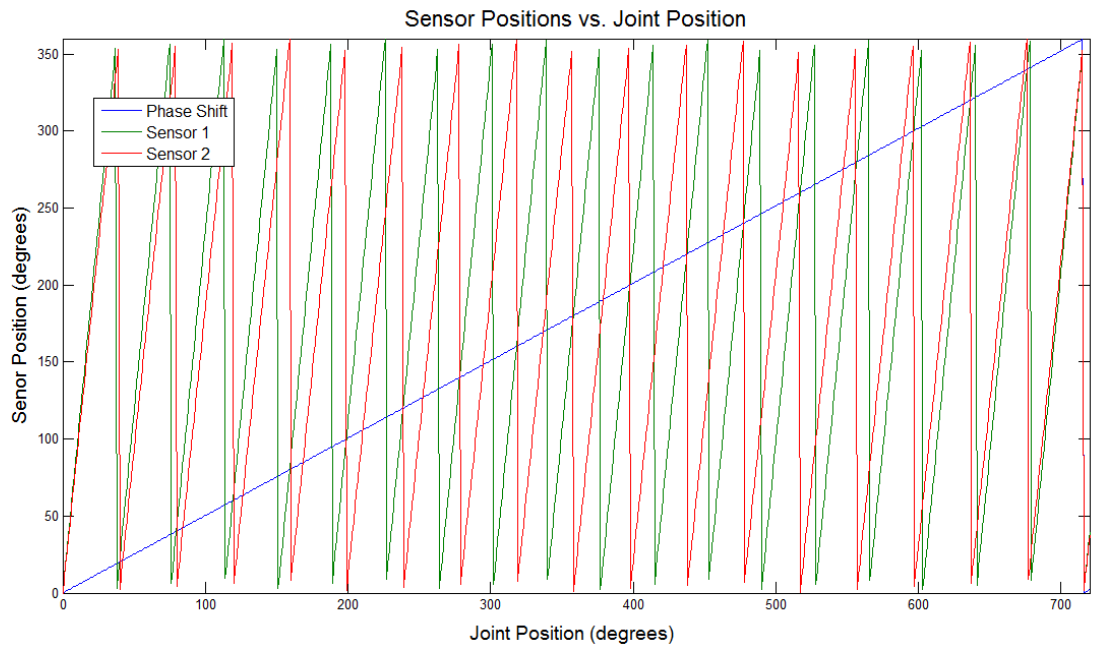


**Figure 4.7** Shoulder flexion joint sensor positions and phase shift between the sensors

## CHAPTER 5

### CONTROLLER DESIGN

The uBot will use local impedance controllers at each joint to implement an endpoint Cartesian impedance controller. The local controllers also modulate the joint impedance if contact is made in locations other than the end effector. This is important when working in unconstrained environments where collisions are likely to occur. This control system will be realized through the implementation of a distributed embedded system where the local impedance controllers are run at the corresponding joint and a Cartesian impedance controller is run at a centralized source to modulate end point impedance. This will not only allow for fast, reliable local joint impedance controllers to be implemented, but also reduces the number of wires running throughout the kinematic chain and thus eliminating failure points [15].

Nomenclature	
Variable	Meaning
$Z_D$	Corresponds to desired impedance parameters $K_z$ , $D_z$ , and $J_z$
$\theta_D$	Desired position
$\theta_e$	Deviation from the desired position
$T_D$	Desired torque calculated by the impedance controller
$\theta_L$	Measured output link angle
$\theta_S$	Measured spring angle
$T_m$	Motor torque
$T_l$	Link torque
$T_{ld}$	Desired link torque
$K_s$	Spring constant

## 5.1 System Model

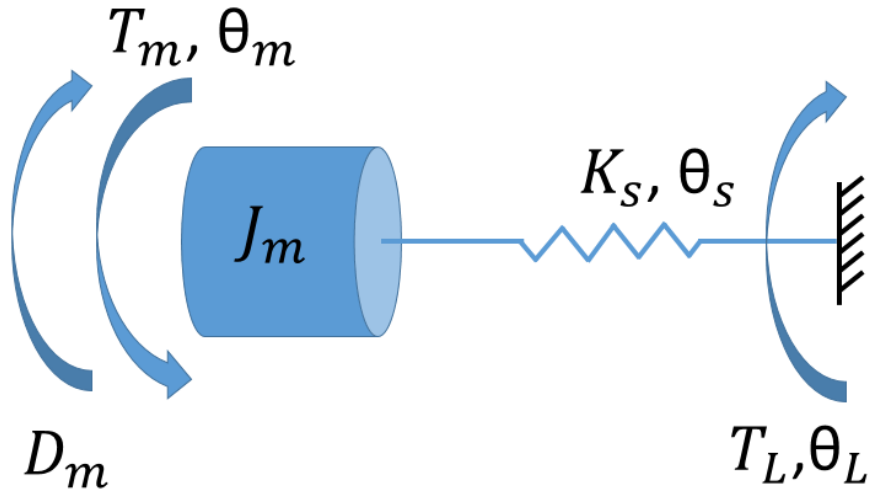


**Figure 5.1** SEA Model used to derive equations of motion

To determine the equations of motion for the SEA the output of the joint was assumed to be locked. This assumption was made because this configuration ensures damping in the system has repeatable effects. Also, the effects of damping will increase with link velocity and therefore this is the most unstable configuration a single joint will see. This is representative of when the manipulator contacts the outside environment. From the SEA schematic shown in Figure 5.1, the following equations can be obtained relating motor torque and link torque:

$$J_m \ddot{\theta}_m = T_m - D_m \dot{\theta}_m - k_s \theta_s \quad (5.1)$$

$$T_L = k_s \theta_s \quad (5.2)$$

$$\theta_m = \theta_L - \theta_s \quad (5.3)$$

## 5.2 Impedance Controller

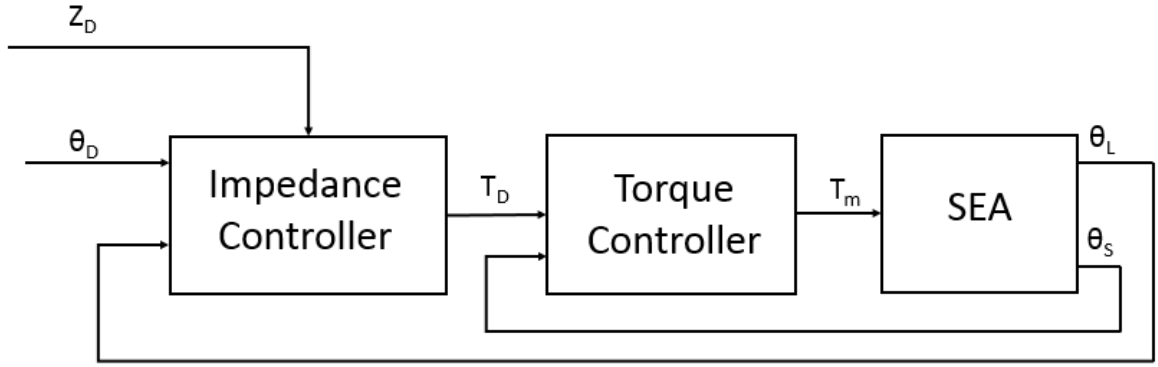


**Figure 5.2** Impedance Controller Structure

An impedance controller was used with the structure shown in Figure 5.2 where the impedance control block consists of the transfer function shown in equation (5.4) and  $\vartheta_e$  is the difference between desired position and measured position.  $K_z$ ,  $D_z$ , and  $J_z$  are variables whose values can be specified to attain desired impedance. As can be seen, the impedance controller is limited by the performance of the embedded torque controller and thus a stable torque controller is necessary.

$$\frac{T_D}{\theta_e} = K_z + D_z s + J_z s^2 \quad (5.4)$$

### 5.3 Torque Controller

The torque controller block consists of two major portions: a part that attempts to compensate for the systems dynamics and a PID controller. From the motor and spring dynamics shown in equations(5.1), (5.2), and (5.3), the following can be derived where  $T_{LD}$  is desired link torque:

$$T_m = T_{LD} + [J_m s^2 + D_m s] \theta_L - [J_m s^2 + D_m s] \theta_s \quad (5.5)$$

This equation holds true in an ideal case, but since there is backlash present in the gearhead and the sensors are subject to noise it is more stable to measure motor position directly and use the following equation where equation (5.3) is substituted into equation(5.5):

$$T_m = T_{LD} + [K_{Jm} J_m s^2 + K_{Dm} D_m s] \theta_m \quad (5.6)$$

It is also important that, as done in [20], gains  $K_{Jm}$  and  $K_{Dm}$ , that are between 0 and 1 are multiplied times the  $J_m$  and  $D_m$  terms respectively to prevent feedback inversion and instability [20]. Notice that, in order to implement this control law, motor velocity and acceleration feedback must be available.

The second portion of the torque controller is the feedback portion which is used to reduce errors created from a non-perfect model. In this case, a PID controller was used with the following form:

$$T_m = [T_{LD} - k \theta_s] [k_d s + k_p + \frac{k_i}{s}] \quad (5.7)$$

Combining these controllers the following control law can be derived:

$$T_m = [T_{LD} - k \theta_s] [k_d s + k_p + \frac{k_i}{s}] + T_{LD} + [K_{Jm} J_m s^2 + K_{Dm} D_m s] \theta_m \quad (5.8)$$

This is similar to the control law used in [20] except  $\vartheta_s$  is measured directly and can therefore be compensated for through feedback, and the motor damping is canceled.

## 5.4 Controller Hardware

The local joint controllers run the local impedance control loops based on set parameters received from the master. This reduces the computational load on the master controller. The local controllers do not need to be updated at every time step and therefore it is not necessary for the master controller to run at the same frequency as the local controllers. It is also possible for the local controllers to maintain stability even if errors occur in the master controller and it does not send updated set points.

The local joint controllers run the joint level impedance control algorithms. The hardware is mainly composed of a microcontroller and a motor controller. The motor controller runs closed loop current control, supplies power to, and commutates the motor. The microcontroller receives set positions and impedances from the master, reads joint sensors, runs the local impedance controller, sends the desired current to the motor controller, and communicates joint states back to the master. A schematic of the local joint controller is shown in Figure 5.3 where the components inside the dotted green line are at each joint and the communication bus runs from the master to all joints. The communication bus can also be seen in the uBot-7 embedded system outline shown in Figure 3.26. This hardware was implemented on the SEA prototype with a MicroChip PIC32MX795F512L for a microcontroller and an ESCON Module 50/5 motor controller from Maxon. This motor controller can supply a maximum current of 15 amps and a continuous current of 5 amps which is higher than the continuous current rating of the motors used and thus the motor controller capability does not limit the

joint torque. Further work beyond this thesis will be put into developing the communication protocol and implementing the system on the robot.

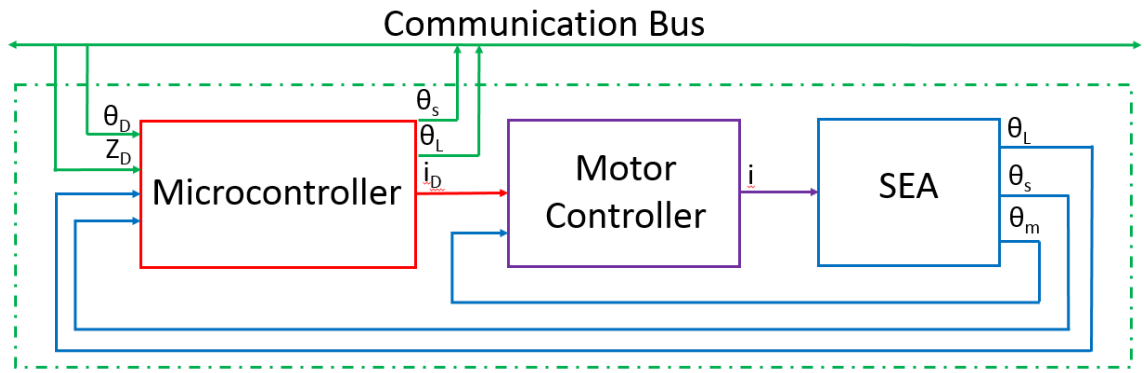


**Figure 5.3** Proposed schematic of local joint controller hardware structure

## CHAPTER 6

### IMPLEMENTATION AND EXPERIMENTS

#### 6.1 Torque Controller Evaluation

To implement the torque controller shown in equation(5.8), spring deflection and motor position must be measured. In the SEA prototype motor velocity was measured with the Hall effect sensors on the motor. This signal went to the motor controller which then passed as an analog signal to the microcontroller where the torque control loop operates. This analog motor velocity signal proved to be too noisy to be accurately differentiated to get acceleration at the controller frequency of 1000Hz and therefore was not used to compensate for the motor inertia. It was also found that compensating for the system damping has positive effects of increasing force control accuracy in non-zero velocity scenarios but negatively affected the stability of the system and was therefore not used. For these reasons the following torque control law was implemented with gains of  $K_p=5$  and  $K_i=0.002$ :

$$T_m = T_{ID} + [T_{ID} - k_s \theta_s][K_p + \frac{K_i}{s}] \quad (5.9)$$

This frequency response of this controller tested on the SEA prototype and can be seen in Figure 6.1 where the input signal was a sine wave about 0 with an amplitude of 1, 2, and 4 Nm. In these tests the output of the joint was locked. An open loop controller was also plotted to provide a baseline to compare to. Notice that the bandwidth of this system is between 20 and 30 rad/sec. This is to be expected as it is slightly above the systems natural frequency of ~20 rad/sec.



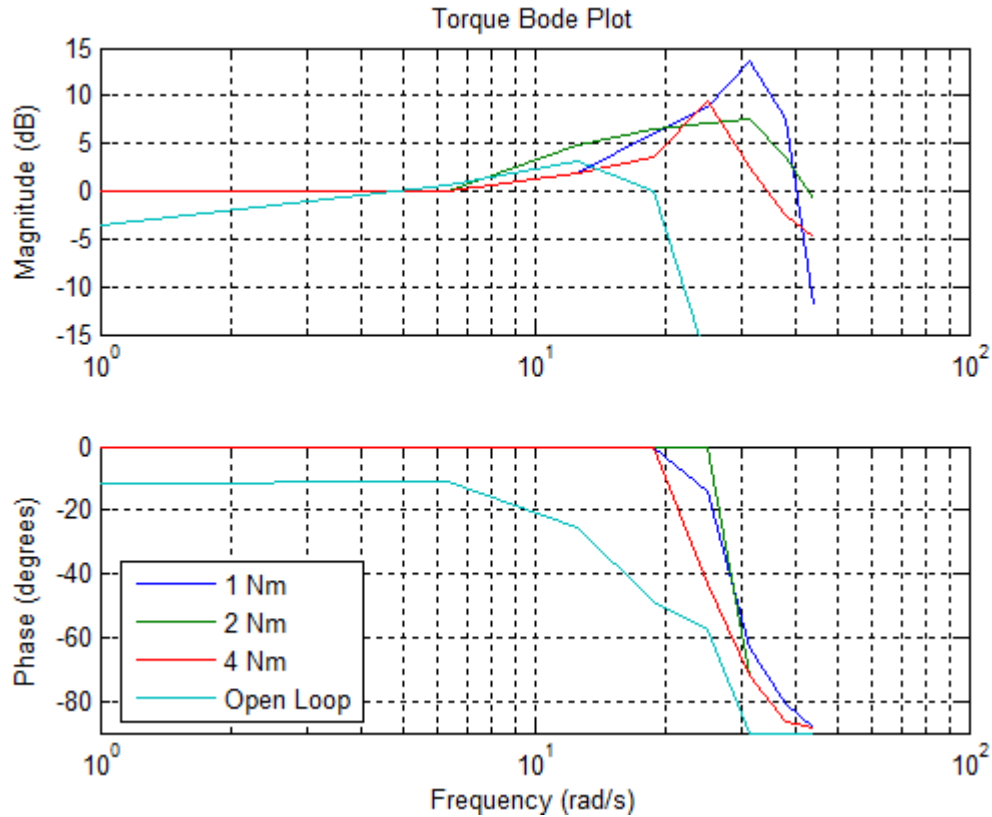


**Figure 6.1** Torque Bode plot of SEA prototype with an input signal that has a magnitude of 1 Nm, 2 Nm, 4 Nm, and with only an open loop controller

As shown in [46], raising the systems natural frequency raises the open loop control bandwidth. To test if this would increase the closed loop torque control bandwidth a new spring was fabricated with a spring constant of  $7.2 \text{ Nm/}^\circ$ . The frequency response of this, as compared to the original spring constant, can be seen in Figure 6.2. Notice that the cutoff frequencies are close for these two plots. This proves that even though raising the spring constant increase the systems natural frequency, it does not in fact increase the closed loop bandwidth for this system. This is likely due to the fact that sensor noise, and system non-linearity's all remain constant. Also, at higher spring constants torque sensing resolution decreases. It was also observed that, at higher frequencies, the backlash causes a non-linear and unpredictable behavior. This was partly due to the torque response of the motor without inertial and frictional

compensation. At high frequencies the motor would only leave backlash region a fraction of the time. As previously stated, this is a research platform and further exploration of the effect of spring constants can be studied in the future.

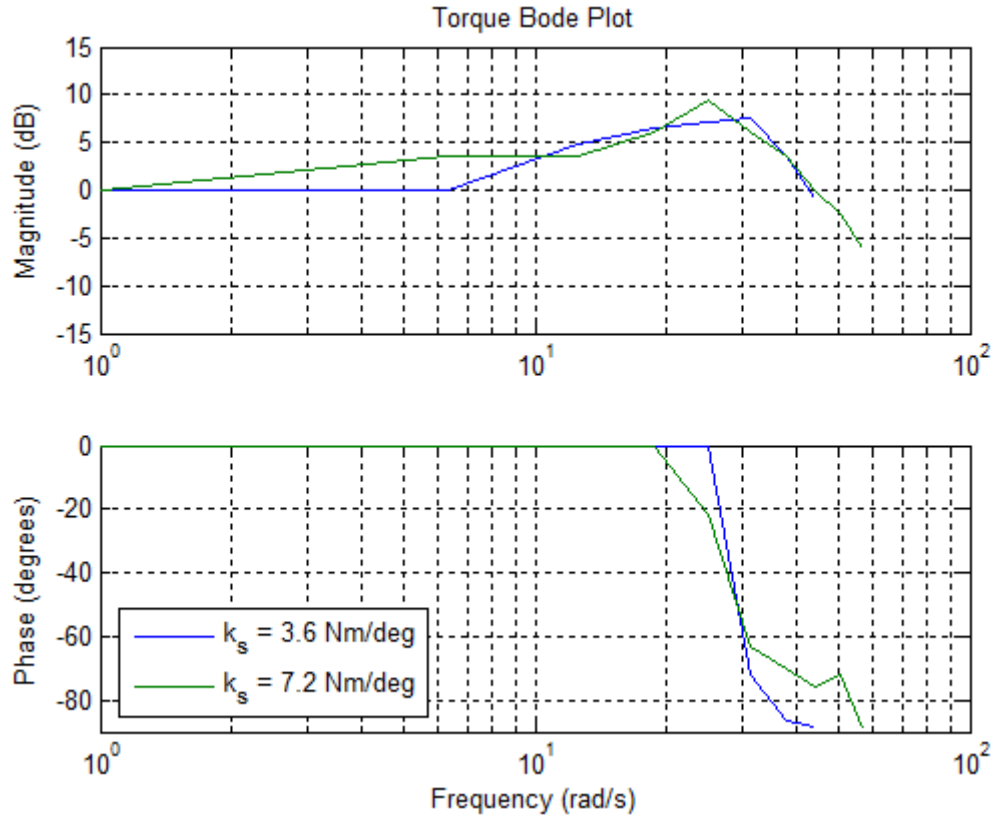


**Figure 6.2** Torque Bode plot of SEA prototype with spring constants of 3.6 Nm/° and 7.2 Nm/°

To test what effects backlash had on the system, a frequency response was generated in a situation where backlash was not present. This was done by using a sine wave that was offset such that no zero crossing occurred as the input signal. This kept the system torque in one direction and thus remained out of the backlash zone. For this test the 3.6 Nm/° spring was used and a sine wave with a 1 Nm magnitude was offset to 5 Nm ( $T_D = 5 + \sin(\omega)$ ). The result of this can be seen in Figure 6.3. Notice that the bandwidth is raised from ~20 rad/sec to ~25 rad/sec and the system has a lower peak

magnitude at resonance. In most situations the uBot-7 will operate in such a way that desired joint torques are non-zero and thus backlash effects will not always reduce performance. It is also important to notice the slight phase shift and negative magnitude gain at low frequencies. This appeared to be from effects of friction and stiction that increased with torque.

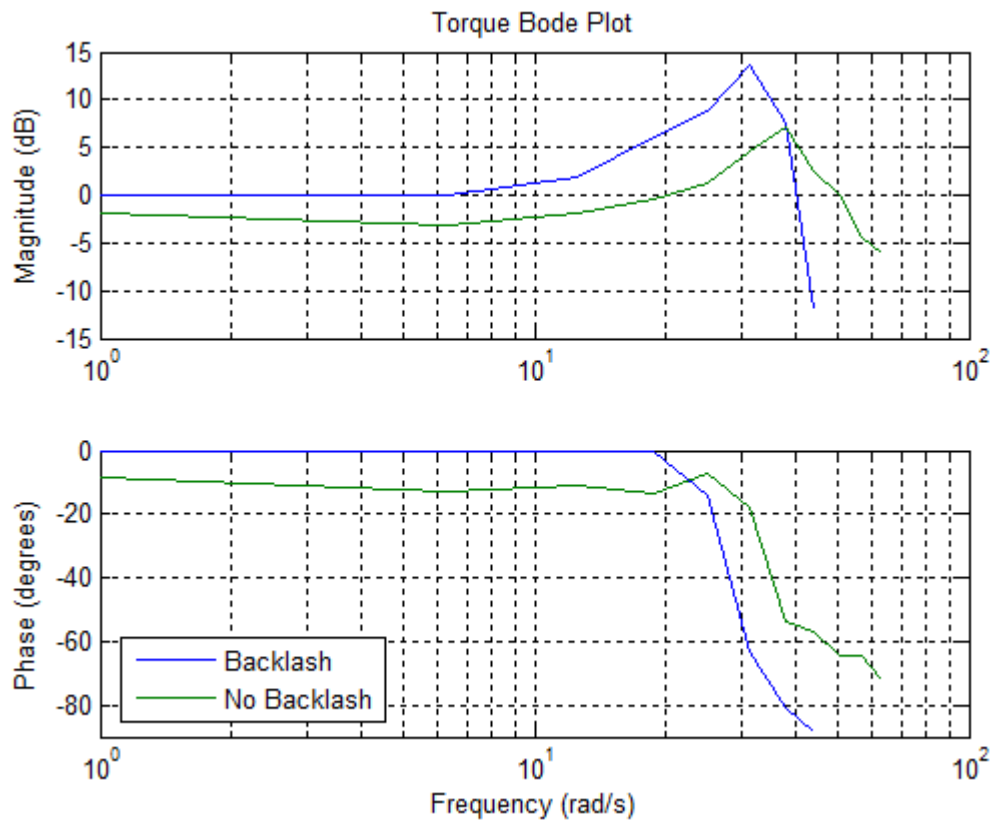


**Figure 6.3** Torque Bode plot of actuator with 1 Nm magnitude sine wave centered at zero causing backlash and centered at 5 Nm eliminating backlash

The bandwidth could be increased with the implementation of better motor velocity and acceleration feedback that have less noise allowing  $J_m$  and  $D_m$  to be compensated. It can also be increased by using larger feedback gains, however, this can lead to instabilities due to

nonlinearities in the system such as backlash and stiction. The reduction of deflection sensor noise may also increase the bandwidth.

## 6.2 Impedance Controller Evaluation

Testing the impedance controller proved that a large range of stiffness impedance parameters ( $k_z$ ) produced controllable results ranging from 18 mNm/deg to 360 mNm/deg, or  $1/200^{\text{th}}$  to  $1/10^{\text{th}}$  of the physical spring constant. Higher stiffnesses produced unstable behaviors, however this was not extensively studied in this thesis. The first order impedance used was 5 mNmS/deg as this produced reasonable damping effects and higher values of  $D_z$  resulted in unstable behavior due to sensor noise.  $J_z$  was also not implemented due to sensor noise.

Figure 6.4 shows two sine wave position trajectories of  $\frac{1}{2}$  Hz and 1 Hz frequency being followed by a high and a low impedance controller of  $K_z=360$  mNm/degree and 36 mNm/degree respectively.  $D_z=5$  mNmS/degree was used in both cases. At  $\frac{1}{2}$  Hz the high impedance controller follows the trajectory very closely and the low impedance controller has a slight increase in magnitude and phase lag. This is to be expected because the lower impedance controller is behaving in a similar manner to a soft spring. At 1 Hz, both the impedance modes show deviations from the trajectory. In this case, the high impedance controller actually shows larger deviations from the trajectory. This is likely to be due to resonations at this frequency. These plots show the importance of picking the correct impedance for the correct situation. In situations where precise position control is important higher impedance should be chosen. It is also important to be aware of what causes resonance with the choice of a controller. This being said, a detailed study of correlating resonance to impedance was not explored in this work.

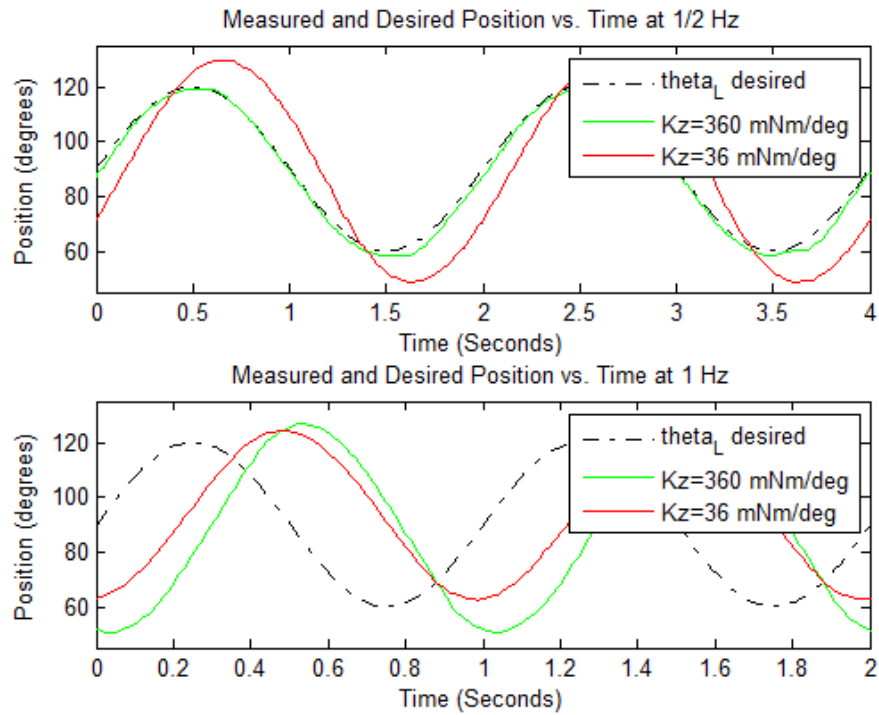


**Figure 6.4** Trajectory following at 1/2 Hz (top) and 1 Hz (bottom) with high and low impedances of  $K_z=360$  mNm/deg and  $K_z=36$  mNm/deg and a damping coefficient of  $D_z=5$  mNmS/deg



**Figure 6.5** The SEA prototype with an object obstructing its trajectory (left) and after the object has been moved when using high impedance (right)

To test how the impedance controller behaves upon contact, an experiment was done where an object was placed such that it obstructed the joints desired trajectory. This can be seen in Figure 6.5 where the picture on the left was taken just before contact was made. The assigned trajectory was a 1/4 Hz sine wave. Figure 6.6 shows the measured and desired positions

and torques for this experiment. Note that the range of torques plotted,  $\pm 12\text{Nm}$ , corresponds to the range of torques the actuator is capable. At  $t = 5$  seconds the joint makes contact with the obstacle. In the case of the high impedance controller, upon contact there is a slight deviation from the desired trajectory and the torque rises. The object is then pushed out of the way and the joint remains close to its set path. This can be seen in Figure 6.5 where the picture on the left was taken just before contact is made and the picture on the right shows the object moved out of the way. This same test was done with a much lower impedance of  $18\text{ mNm/deg}$ . In this case the actuator does not move the obstacle upon contact as can be seen on the right side of Figure 6.6 where contact is made at 5 seconds. Because of the low impedance parameters chosen, the torque remains low even at large position deviations. It can also be seen in this figure that effects of stiction are prevalent when that actuator changes direction.

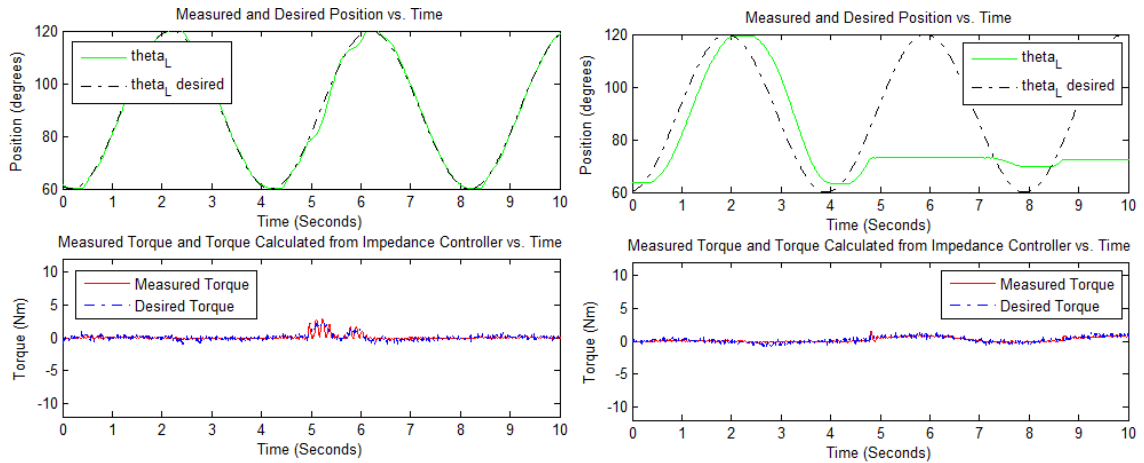


**Figure 6.6**  $\frac{1}{4}$  Hz trajectory following with  $K_z=360\text{ mNm/deg}$ ,  $D_z=5\text{mNmS/deg}$  (left) and  $K_z=18\text{ mNm/deg}$ ,  $D_z=5\text{mNmS/deg}$  and a collision at 5 seconds

The final test discussed in this section is the step response of the impedance controller. This is seen in Figure 6.7 where three different impedances were subjected to a  $30^\circ$  and  $90^\circ$  step. The high, medium, and low stiffnesses ( $K_z$ ) used in this case were  $360\text{ mNm/deg}$ ,  $180$

mNm/deg, and 36 mNm/deg. For all of these cases the same damping parameter ( $D_z$ ) of 5 mNmS/degree was used. As expected, the higher stiffnesses resulted in an under-damped response. The low stiffness resembles an over-damped response in the 30° case however it overshoots in the 90° test. This is likely due to the speed the speed at which it was moving. It is also interesting to notice that the in the 90° step all three controllers have a similar rise time. This is due to the fact that the motor has saturated and it cannot reach the desired torque. If an obstacle were introduced to the trajectory, however, they different controllers would function differently as seen in Figure 6.5.

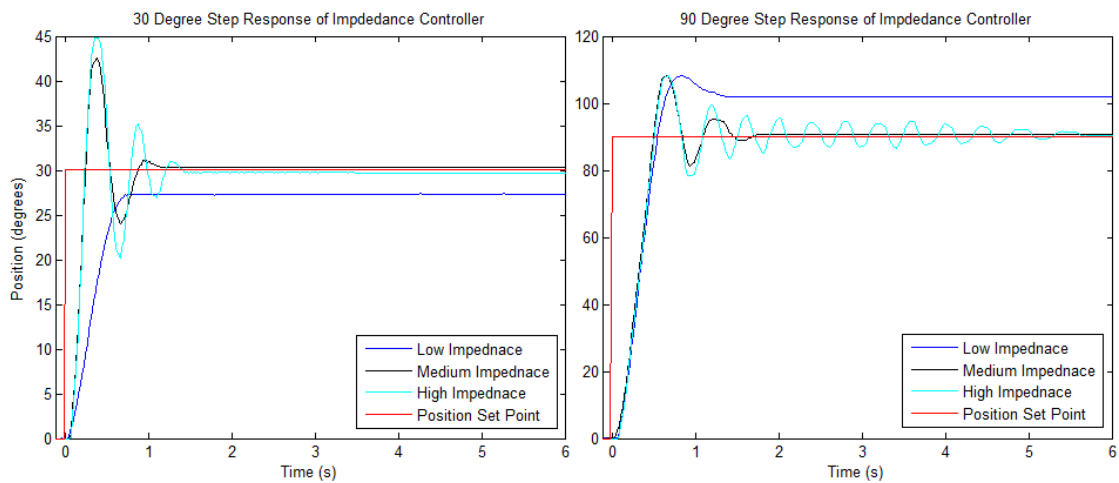


**Figure 6.7** Step response of the impedance controller to a 30° and 90° step at high, medium, and low stiffnesses of 360 mNm/deg, 180 mNm/deg, and 36 mNm/deg



## CHAPTER 7

### RECOMMENDATIONS FOR FUTURE IMPLEMENTATION

The first improvement that can be made is improving the motor position feedback such that accurate motor position can be measured and differentiated to get velocity and acceleration. This work proved that stable torque control can be attained without motor position feedback. This being said, Equation 1.9 shows that if motor velocity and acceleration are known and an accurate motor model has been established then a controller can be implemented to compensate the motor dynamics. This would likely improve the torque controller bandwidth and result in a more robust controller. This would also increase the capability to calibrate the spring deflection sensors as the difference between motor and link position can be measured.

To implement the position feedback, the motor position Hall effect sensors could be read by a microcontroller instead of the motor controller which introduced noise and lag to the signal. These sensors create 24 counts/revolution of the motor which translates to 3816 counts/revolution or  $.09^\circ/\text{count}$  after the gearhead reduction. This would introduce significant load to the microcontroller as the frequency of interrupts would be very high. The second option would be to get encoders for the motor which would offer higher resolution and could be implemented on a microcontroller with dedicated encoder modules.

Secondly, higher frequency sensors would improve the sensing and/or controller performance. They would allow the local control loops to run faster. Currently, they run at 1000 Hz which has been proven to work but performance could be increased with a faster control loop. Due to the controller structure (shown in Figure 5.2) the outer (impedance) control loop can only run as fast as the inner (torque) control loop. The reverse of this is possible where the torque loop runs faster, however, and could be done if the spring deflection sensor could run at

a higher frequency. Higher frequency sensors can also be used at the same controller frequency but instead used to decrease sensor noise. This can be done by averaging or filtering signals of the sensor. One way to accomplish this is to use an analog sensor. The microcontroller used to run the local control loop (PIC32MX795F512L) can read an analog signal at frequencies of 1 MHz which far exceeds the current 1000 Hz frequency. Using an analog sensor would also allow for an analog low pass filter with a cutoff frequency slightly above the controller frequency to be implemented. This would minimize the effect of noise as compared to the current sensor.

Once the uBot-7 platform is operational, there will be opportunities to optimize the platforms control parameters and spring constants. One potential way to do this could be to explore the systems resonant frequencies as done in [42] which experiments with “hopping” using COMAN. For the uBot platform optimizations could be done focusing on energy dissipation in a fall or reactions to disturbances while balancing.

Due to the timeline and resources allocated to this project, finite element analysis based optimizations with respect to minimizing weight were not extensively done. Focus on this would improve the robots weight and inertia. This would have the positive effect of improving the systems efficiency, speed, and safety.

One more optimization that could be done would be to explore the optimal reductions used in the joints with respect to predefined tasks. This would be especially interesting because the motor controllers are capable of supplying 15 A of current intermittently. The current design focused on continuous torques but models could be made to utilize intermittent torque region operation for short periods of time which are currently avoided entirely.

## **CHAPTER 8**

### **CONCLUSION**

As the need to apply robots to a wider range of situations increases, the approach to building and controlling robots must change to accommodate these new needs. Fast and precise position controlled robots have been shown to be very effective in a controlled environment such as a factory, however, they do not meet the needs of robots that operates in highly variable and poorly modeled environments where humans may be present.

This thesis presented the new design of the uBot with the objective of increasing the robots capability to function dexterously, through the incorporation of joint torque feedback, and safely, through the implementation of passive and active compliance. To accomplish this some major changes to the platform were made. These changes include: the addition of series elastic actuators (SEAs) to the arms and torso joints, joint level impedance control algorithms, a distributed embedded system, and a low backlash drivetrain mechanism. The uBot was developed as a low cost solution to whole body dexterity and mobile manipulation and thus the SEA design for uBot-7 fits within these criteria. This thesis discusses the development of the actuator mechanics, sensors, and control based on these criteria. This process provides insight into how to extend this design to other applications. A local joint impedance and torque controller was also developed for this design and tested on a 1 DOF prototype. The evaluation of this system showed that a wide range of impedances can be implemented on this joint. Precise trajectory following as well as low impedance can be achieved through the correct choice of impedance parameters.

The future of this project will involve designing the distributed embedded control system for the robot including both the electrical system and communication protocol. Once

this is complete an endpoint impedance controller can be implemented and new avenues for whole body dexterity, dexterous mobility, and manipulation can be explored.

## APPENDIX

### EXPERIMENTAL PARAMETER VALUES

#### TORQUE BODE PLOT (page 76)

Closed control law:

$$T_m = T_{ID} + [T_{ID} - k_s \theta_s][K_p + \frac{K_i}{s}]$$

Input:

1 Nm:  $T_{ID} = \sin(f)$

2 Nm:  $T_{ID} = 2 \sin(f)$

4 Nm:  $T_{ID} = 4 \sin(f)$

Parameters used:

$$k_s = 3.6 Nm / \text{deg}$$

$$K_p = 5$$

$$K_i = 0.002$$

Open loop control law:

$$T_m = T_{ID}$$

Input:

$$T_{ID} = 2 \sin(f)$$

#### TORQUE BODE PLOT WITH ADJUSTED $K_s$ (page 77)

Closed control law:

$$T_m = T_{ID} + [T_{ID} - k_s \theta_s][K_p + \frac{K_i}{s}]$$

Input:

$$T_{ID} = 2 \sin(f)$$

Parameters used:

$$k_s = 3.6 Nm / \text{deg}$$

$$k_s = 7.2 Nm / \text{deg}$$

$$K_p = 5$$

$$K_i = 0.002$$

### TORQUE BODE PLOT WITHOUT BACKLASH (page 78)

Closed control law:

$$T_m = T_{ID} + [T_{ID} - k_s \theta_s][K_p + \frac{K_i}{s}]$$

Input:

$$T_{ID} = \sin(f)$$

And

$$T_{ID} = 5 + \sin(f)$$

Parameters used:

$$k_s = 3.6Nm / \text{deg}$$

$$K_p = 5$$

$$K_i = 0.002$$

### TRAJECTORY FOLLOWING WITH IMPEDANCE CONTROL (page 81)

Torque control law:

$$T_m = T_{ID} + [T_{ID} - k_s \theta_s][K_p + \frac{K_i}{s}]$$

Impedance control law:

$$T_D = K_z \theta_e + D_z s \theta_e$$

Input:

$$\theta_{ID} = \sin(2\pi)$$

And

$$\theta_{ID} = \sin(\pi)$$

Parameters used:

$$k_s = 3.6Nm / \text{deg}$$

$$K_p = 5$$

$$K_i = 0.002$$

$$K_z = 36mNm / \text{deg}$$

$$K_z = 360mNm / \text{deg}$$

$$J_z = 5mNmS / \text{deg}$$

## COLLISION WITH IMPEDANCE CONTROL (page 82)

Torque control law:

$$T_m = T_{ID} + [T_{ID} - k_s \theta_s][K_p + \frac{K_i}{s}]$$

Impedance control law:

$$T_D = K_z \theta_e + D_z s \theta_e$$

Input:

$$\theta_{ID} = \sin(2\pi / 4)$$

Parameters used:

$$k_s = 3.6 Nm / \text{deg}$$

$$K_p = 5$$

$$K_i = 0.002$$

$$K_z = 18 mNm / \text{deg}$$

$$K_z = 360 mNm / \text{deg}$$

$$J_z = 5 mNmS / \text{deg}$$

## STEP RESPONSE WITH IMPEDANCE CONTROL (page 83)

Torque control law:

$$T_m = T_{ID} + [T_{ID} - k_s \theta_s][K_p + \frac{K_i}{s}]$$

Impedance control law:

$$T_D = K_z \theta_e + D_z s \theta_e$$

Input:

$$\theta_{ID} = \sin(2\pi / 4)$$

Parameters used:

$$k_s = 3.6 Nm / \text{deg}$$

$$K_p = 5$$

$$K_i = 0.002$$

$$K_z = 36 mNm / \text{deg}$$

$$K_z = 180 mNm / \text{deg}$$

$$K_z = 360 mNm / \text{deg}$$

$$J_z = 5 mNmS / \text{deg}$$

## REFERENCES

- [1] R. Ambrose, B. Wilcox, B. Reed, L. Matthies, D. Lavery, and D. Kormeyer, "Robotics, Tele-Robotics and Autonomous Systems Roadmap Technology Area 04." National Aeronautics and Space Administration, 2012.
- [2] G. I. of Technology, C. M. University, R. T. Consortium, U. of Pennsylvania, U. of S. California, S. University, U. of California–Berkeley, U. of Washington, and M. I. of Technology, "A Roadmap for U . S . Robotics." 2013.
- [3] A. M. Okamura, N. Smaby, and M. R. Cutkosky, "An Overview of Dexterous Manipulation," in *Proceedings of the 2000 IEEE International Conference on Robotics & Automation San Francisco, CA April 2000*, 2000, no. April.
- [4] S. R. Kuindersma, E. Hannigan, D. Ruiken, and R. A. Grupen, "Dexterous Mobility with the uBot-5 Mobile Manipulator," in *Proceedings of the 14th International Conference on Advanced Robotics (ICAR)*, 2009.
- [5] D. Ruiken, M. W. Lanighan, and R. A. Grupen, "Postural Modes and Control for Dexterous Mobile Manipulation : the UMass uBot Concept," in *In Proceedings of the 13th IEEE-RAS International Conference on Humanoid Robots. Atlanta, Georgia, October 2013.*, 2014.
- [6] D. Ruiken, M. W. Lanighan, and R. A. Grupen, "Path Planning for Dexterous Mobility," in *Proceedings of the 24th International Conference on Automated Planning and Scheduling (ICAPS). Portsmouth, New Hampshire*, 2014.
- [7] G. Konidaris, S. Kuindersma, R. Grupen, and A. Barto, "Autonomous Skill Acquisition on a Mobile Manipulator," in *In Proceedings of the Twenty-Fifth Conference on Artificial Intelligence (AAAI-11)*, 2011.
- [8] G. Konidaris, C. Ma, S. Kuindersma, R. Grupen, and A. Barto, "Acquiring Transferrable Mobile Manipulation Skills," in *RSS 2011 Workshop on Mobile Manipulation: Learning to Manipulate, Los Angeles, CA*, 2011.
- [9] H. Jung, T. Takahashi, and R. Grupen, "Human-Robot Emergency Response - Experimental Platform and Preliminary Dataset Technical Report # UM-CS-2014-006," 2014.
- [10] H.-T. Jung, Y.-K. Choe, J. Baird, and R. a. Grupen, "A follow-up on humanoid-mediated stroke physical rehabilitation," *Proc. seventh Annu. ACM/IEEE Int. Conf. Human-Robot Interact. - HRI '12*, p. 159, 2012.
- [11] Y. Choe, H.-T. Jung, J. Baird, and R. a. Grupen, "Multidisciplinary stroke rehabilitation delivered by a humanoid robot: Interaction between speech and physical therapies," *Aphasiology*, vol. 27, no. 3, pp. 252–270, Mar. 2013.



- [12] H.-T. Jung, J. Baird, Y.-K. Choe, and R. a. Grupen, "Upper extremity physical therapy for stroke patients using a general purpose robot," *2011 Ro-Man*, pp. 270–275, Jul. 2011.
- [13] H.-T. Jung, T. Takahashi, Y.-K. Choe, J. Baird, T. Foster, and R. a. Grupen, "Towards extended virtual presence of the therapist in stroke rehabilitation.," *IEEE Int. Conf. Rehabil. Robot.*, vol. 2013, p. 6650345, Jun. 2013.
- [14] G. A. Pratt and M. M. Williamson, "Series Elastic Actuators," in *Intelligent Robots and Systems 95*, 1995.
- [15] M. A. Diftler, J. S. Mehling, M. E. Abdallah, N. A. Radford, L. B. Bridgwater, A. M. Sanders, R. S. Askew, D. M. Linn, J. D. Yamokoski, F. A. Permenter, B. K. Hargrave, R. Platt, R. T. Savely, R. O. Ambrose, G. Motors, and O. S. Systems, "Robonaut 2 – The First Humanoid Robot in Space," in *2011 IEEE International Conference on Robotics and Automation*, 2011, vol. 1, pp. 2178–2183.
- [16] B. J. Thibodeau, P. Deegan, and R. Grupen, "Static analysis of contact forces with a mobile manipulator," *Proc. 2006 IEEE Int. Conf. Robot. Autom. 2006. ICRA 2006.*, pp. 4007–4012, 2006.
- [17] "7 Newest Robot Generations and Their Uses." [Online]. Available: <http://www.pouted.com/7-newest-robots-generations-uses/>.
- [18] S. Kuindersma, R. Grupen, and A. Barto, "Learning dynamic arm motions for postural recovery," *2011 11th IEEE-RAS Int. Conf. Humanoid Robot.*, pp. 7–12, Oct. 2011.
- [19] FAULHABER, "Micromo 30/1s Planetary Gearhead Datasheet," 2014. [Online]. Available: <http://www.micromo.com/precision-gearheads-datasheets>.
- [20] G. a. Pratt and M. M. Williamson, "Series elastic actuators," *Proc. 1995 IEEE/RSJ Int. Conf. Intell. Robot. Syst. Hum. Robot Interact. Coop. Robot.*, vol. 1, pp. 399–406, 1995.
- [21] N. G. Tsagarakis, M. Laffranchi, B. Vanderborght, and D. G. Caldwell, "A compact soft actuator unit for small scale human friendly robots," *2009 IEEE Int. Conf. Robot. Autom.*, pp. 4356–4362, May 2009.
- [22] N. G. Tsagarakis, J. Saglia, and D. G. Caldwell, "The design of the lower body of the compliant humanoid robot 'cCub,'" *2011 IEEE Int. Conf. Robot. Autom.*, pp. 2035–2040, May 2011.
- [23] N. G. Tsagarakis, B. Vanderborght, M. Laffranchi, and D. G. Caldwell, "The mechanical design of the new lower body for the child humanoid robot 'iCub,'" *2009 IEEE/RSJ Int. Conf. Intell. Robot. Syst.*, pp. 4962–4968, Oct. 2009.
- [24] C. Lagoda, A. C. Schouten, A. H. A. Stienen, E. E. G. Hekman, and H. Van Der Kooij, "Design of an electric Series Elastic Actuated Joint for robotic gait rehabilitation training,"

in *Proceedings of the 2010 3rd IEEE RAS & EMBS International Conference on Biomedical Robotics and Biomechatronics*, 2010, pp. 21–26.

- [25] N. Paine, S. Member, S. Oh, L. Sentis, and A. S. E. A. D. Background, “Design and Control Considerations for High-Performance Series Elastic Actuators,” *IEEE/ASME Trans. MECHATRONICS*, pp. 1–12, 2014.
- [26] S. Wang, C. Meijneke, and H. van der Kooij, “Modeling, design, and optimization of Mindwalker series elastic joint.,” *IEEE Int. Conf. Rehabil. Robot.*, vol. 2013, p. 6650381, Jun. 2013.
- [27] G. Wyeth, “Control Issues for Velocity Sourced Series Elastic Actuators,” in *Proceedings of the Australasian Conference on Robotics and Automation 2006*, 2006.
- [28] I. Thorson and D. Caldwell, “A nonlinear series elastic actuator for highly dynamic motions,” *2011 IEEE/RSJ Int. Conf. Intell. Robot. Syst.*, pp. 390–394, Sep. 2011.
- [29] K. Kong, J. Bae, S. Member, and M. Tomizuka, “A Compact Rotary Series Elastic Actuator for Human Assistive Systems,” vol. 17, no. 2, pp. 288–297, 2012.
- [30] K. Kong, S. Member, and J. Bae, “Control of Rotary Series Elastic Actuator for Ideal Force-Mode Actuation in Human – Robot Interaction Applications,” *IEEE/ASME Trans. MECHATRONICS*, vol. 14, no. 1, pp. 105–118, 2009.
- [31] J. Sensinger and R. Ff. Weir, “Improvements to Series Elastic Actuators,” in *2006 2nd IEEE/ASME International Conference on Mechatronics and Embedded Systems and Applications*, 2006, pp. 1–7.
- [32] T. Deyle, “Baxter Robot from Rethink Robotics Finally Unveiled!,” 2012. .
- [33] L. B. Bridgwater, C. a Ihrke, M. a Diftler, N. a Radford, J. M. Rogers, S. Yayathi, D. M. Linn, and G. Motors, “The Robonant 2 Hand - Designed To Do Work With Tools,” *Int. Conf. Robot. Autom.*, pp. 3425–3430, 2012.
- [34] Z. Li, N. G. Tsagarakis, and D. G. Caldwell, “A passivity based admittance control for stabilizing the compliant humanoid COMAN,” in *2012 12th IEEE-RAS International Conference on Humanoid Robots (Humanoids 2012)*, 2012, pp. 43–49.
- [35] Z. Li, N. G. Tsagarakis, and D. G. Caldwell, “Walking pattern generation for a humanoid robot with compliant joints,” *Auton. Robots*, vol. 35, no. 1, pp. 1–14, Apr. 2013.
- [36] Z. Li, N. G. Tsagarakis, and D. G. Caldwell, “Walking trajectory generation for humanoid robots with compliant joints: Experimentation with COMAN humanoid,” in *2012 IEEE International Conference on Robotics and Automation*, 2012, pp. 836–841.

- [37] Z. Li, B. Vanderborght, N. G. Tsagarakis, L. Colasanto, and D. G. Caldwell, "Stabilization for the compliant humanoid robot COMAN exploiting intrinsic and controlled compliance," in *2012 IEEE International Conference on Robotics and Automation*, 2012, pp. 2000–2006.
- [38] N. G. Tsagarakis, S. Morfey, G. Medrano Cerda, L. Zhibin, and D. G. Caldwell, "COMpliant huMANoid COMAN: Optimal joint stiffness tuning for modal frequency control," *2013 IEEE Int. Conf. Robot. Autom.*, pp. 673–678, May 2013.
- [39] L. Colasanto, N. G. Tsagarakis, and D. G. Caldwell, "A compact model for the compliant humanoid robot COMAN," *2012 4th IEEE RAS EMBS Int. Conf. Biomed. Robot. Biomechatronics*, pp. 688–694, Jun. 2012.
- [40] F. L. Moro, N. G. Tsagarakis, and D. G. Caldwell, "Efficient Human-Like Walking for the Compliant huMANoid COMAN based on Kinematic Motion Primitives ( kMPs )," pp. 2007–2014, 2012.
- [41] F. L. Moro, N. G. Tsagarakis, and D. G. Caldwell, "A human-like walking for the COMpliant huMANoid COMAN based on CoM trajectory reconstruction from kinematic Motion Primitives," *2011 11th IEEE-RAS Int. Conf. Humanoid Robot.*, pp. 364–370, Oct. 2011.
- [42] B. Ugurlu, J. a. Saglia, N. G. Tsagarakis, and D. G. Caldwell, "Hopping at the resonance frequency: A trajectory generation technique for bipedal robots with elastic joints," *2012 IEEE Int. Conf. Robot. Autom.*, pp. 1436–1443, May 2012.
- [43] Chris Ihrke; Joashua Mehling ; Adam H. Parsons; Bryan Kristian Grif; Nicolaus A. Radford; Frank Noble Permenter; Donald R. Davis; Robert O. Ambrose, "ROTARY SERIES ELASTIC ACTUATOR Patent No .: US 8,291,788 B2," 2012.
- [44] A. Steel, "17-4 PH STAINLESS STEEL," 2007. [Online]. Available: [http://www.aksteel.com/pdf/markets\\_products/stainless/precipitation/17-4\\_PH\\_Data\\_Sheet.pdf](http://www.aksteel.com/pdf/markets_products/stainless/precipitation/17-4_PH_Data_Sheet.pdf).
- [45] G. Tonietti and A. Bicchi, "Fast and 'Soft-Arm' Tactics," no. June, 2004.
- [46] D. W. Robinson, J. E. Pratt, D. J. Paluska, and G. A. Pratt, "Series Elastic Actuator Development for a Biometric Walking Robot," in *Proceedings of the 1999 LEEWASME International Conference on Advanced Intelligent Mechatronics*, 1999.
- [47] Holo-Krome, "Torquing Specification Inch & Metric Fastener Chart." [Online]. Available: <http://www.holo-krome.com/pdf/torquedatachart.pdf>.
- [48] F. Drives, "Keyless Locking Devices." [Online]. Available: [http://www.fennerdrives.com/trantorque/\\_/Trantorque-Mini-12mm/?s=ZnwYmZE4](http://www.fennerdrives.com/trantorque/_/Trantorque-Mini-12mm/?s=ZnwYmZE4).
- [49] SDP/SI, "TAPER BUSHINGS." [Online]. Available: <https://sdp-si.com/eStore/Catalog/PartNumber/S99TBSM10>.

- [50] D. Meeker, *Finite Element Method Magnetics*. Available: <http://www.femm.info/wiki/HomePage>, 2013.